Towards Wearable Platform for Accurate Unconstrained Trunk Motion Tracking Using Inertial and Strain Sensors Data Fusion

by

Ahmad Rezaei

B.A.Sc., University of Tehran, 2016

Thesis Submitted in Partial Fulfillment of the
Requirements for the Degree of
Master of Applied Science

in the
School of Mechatronic Systems Engineering
Faculty of Applied Sciences

SIMON FRASER UNIVERSITY
Fall 2019

Approval

Name: **Ahmad Rezaei**

Degree: **Master of Applied Science**

Title: **Towards Wearable Platform for Accurate Unconstrained Trunk Motion Tracking Using Inertial and Strain Sensors Data Fusion**

Examining Committee: **Chair:** Flavio Firmani
Lecturer

Carlo Menon
Senior Supervisor
Professor

Kamal Gupta
Supervisor
Professor
School of Engineering Science

Siamak Arzanpour
Internal Examiner
Associate Professor

Date Defended: **October 29, 2019**

Ethics Statement

Abstract

The thesis focused on the development of a wearable motion tracking platform employing fiber strain sensors and inertial measurement units through a data fusion algorithm. The development of a smart sleeveless shirt for measuring the kinematic angles of the trunk in complicated 3-dimensional movements was demonstrated. Fiber strain sensors were integrated into the fabric as the sensing element of the system. Furthermore, a novel method for obtaining the kinematic data of joints based on the data from wearable sensors was proposed. More specifically, the proposed method uses the data from two gyroscopes and the smart shirt strain sensors in a combined machine learning-unscented Kalman filter (UKF) data fusion approach to track the three-dimensional movements of a joint accurately. The suggested technique thus avoids the common problems associated with extracting the movement information from accelerometer and magnetometer readings in the presence of disturbances. A study with 12 participants performing an exhaustive set of simple to complex trunk movements was conducted to investigate the performance of the developed algorithm. The results of this study demonstrated that the data fusion algorithm could significantly improve the accuracy of motion tracking in complicated 3-dimensional movements. Future work requires coherently combining both types of sensors in a wearable platform for full-body motion tracking so that the proposed algorithm can be tested in a variety of daily living activities.

Keywords: wearable sensors; fiber strain sensor; IMU; unscented Kalman filter; random forest regressor; wearable motion tracking

Acknowledgements

I would like to thank my supervisor, Dr. Carlo Menon for his guidance throughout my research. I would also like to thank the members of the Menrva research group for their helps for conducting this research. I would like to specially thank my family for all their supports during my study.

Table of Contents

List of Tables

List of Figures

Chapter 1

Introduction

The material of this chapter is excerpted, modified, and reproduced with permission from the following papers that I co-authored:

- A. Rezaei, T.J. Cuthbert, M. Gholami, C. Menon, "Application-Based Production and Testing of a Core-Sheath Fiber Strain Sensor for Wearable Electronics: Feasibility Study of Using the Sensors in Measuring Tri-Axial Trunk Motion Angles", Sensors, vol. 19, no. 19, p. 4288, 2019.
- A. Rezaei, M. Khoshnam, C. Menon, "Towards User-friendly Wearable Platforms for Monitoring Unconstrained Indoor and Outdoor Activities", article in preparation.

Sections of this chapter have been adapted from the above papers to fit the scope and formatting of the thesis.

1.1 Background

Musculoskeletal disorders, specifically low back pain (LBP), plague a large portion of the population in a variety of occupations, including healthcare and social assistance [1]. Chronic LBP is the second leading cause of disability worldwide [2]. Despite its widespread prevalence in many occupations, risk assessment and management of LBP is still controversial [3]. Risk assessment for this disorder is a multifactorial problem that both physical and psychosocial factors contribute to its happening [3, 4]. Among the physical factors, several different factors including frequency and duration of lift/bending, average and maximal weight of lift, pounds lifted/lowered per day/hour, frequency and duration of bending/twisting/static posture, estimation of energy expenditure, body part discomfort survey, perceived effort, length of time employed, prolonged sustained bad posture, peak lumbar shear force, cumulative lumbar compression, cumulative spinal loads, and peak spinal flexion velocity have been suggested as attributable to the LBP [5, 6, 7, 8]. However, there is still an open discussion about the relationship between these factors and the LBP occurrence. This unclear relationship is due to the lack of enough long-term kinematic and kinetic information of the workers so that a clear causal relationship can be established. While performing similar workplace tasks in a lab environment has been a common approach to gather this information; it has been shown that the results of such clinical tests were considerably different from real-life examinations [9]. As a result, *in situ* measurement systems are necessary for injury risk assessment. This highlights the need for unobtrusive systems that allow movement tracking measurements without any interference with the user's daily routine. With the emergence of wearable sensors, they can perform a principal role in solving this problem. Their reliability and accuracy however still need to be studied.

In situ motion tracking application is not limited to the biomedical applications such as LBP prevention. It has a variety of applications in sports such as diagnosis, rehabilitation, physical monitoring, and performance improvement in athletes [10]. Kinematic information measured by wearable sensors provides variables that can help the trainers for training implementation and performance evaluation [11, 12]. Variables such as proper execution of physical movements, number of repetitions of the movements, proper posture during executing a movement, and duration of movements can all be measured having the kinematic information of the body [10]. If the athletes are equipped with sensors that are capable of monitoring the movements in real-time, physiologists and trainers can assess the performance, provide necessary interventions, and reduce the chance of injury occurrence. This shows that the importance of *in situ* motion tracking expands to the different applications, as this information is significantly beneficial.

Current technologies that can track movement accurately are non-wearable systems. Non-wearable systems are considered the gold standard for motion analysis measurements. Electromagnetic tracking, ultrasonic, and optoelectronic motion capture are among the non-wearable systems [13]. These systems are all marker-based and have been used in the lab environment as they provide accurate kinematic data of movement. However, they have limitations that restrict their application in the workplace environment (sophisticated hardware, high cost, non-portable). All movements are required to be performed in the capture space of the optoelectronic or the magnetic field of the electromagnetic systems, which makes the application of these systems spatially limited [3]. These limitations raise the need for developing reliable and accurate wearable motion capture systems employing wearable sensors.

Wearable sensors have been recognized as a promising solution for conducting *in situ* measurements that were previously limited only to the laboratory environments. These sensors are available in various types for measuring physiological and movement data such as heart rate, blood pressure, respiratory rate, muscle activity, kinematic, and kinetic data, which are the most common signals of interest for different applications [14]. The extensive range of potential applications of these sensors is due to the substantial amount of information that can be collected using them. They have been used in sport and training [15, 16], clinical and home rehabilitation [17, 18, 19], health, wellness initiatives, and safety monitoring [20, 21, 22, 23, 24, 25, 26], social interaction improvement [27, 28, 29], and occupational safety and health monitoring. For the last application, wearable sensors measuring movement data are of special interest. They can provide valuable physical activity information for monitoring and preventing LBP, which is among the most costly health care problems in the society today [1].

Employing wearable sensors would overcome the limitations of non-wearable systems. These inexpensive sensors eliminate the spatial limitations of non-wearable devices. Electrogoniometers, capacitive strain-based sensors, textile piezoresistive strain sensors, fiberoptic sensors, accelerometers, and inertial measurement units (IMU) are among the most common wearable sensors [3, 30, 31]. Among these, Electrogoniometers have been the first systems being used as wearable devices. Lumbar Motion Monitor(LMM) and CUELA systems are some of the very earliest devices working based on electrogoniometers [32, 33]. They have been employed in several studies for motion tracking [34, 35, 36] and are shown to have a superior level of accuracy for *in situ* data collections. Hybrid systems have been used more recently in which electrogoniometers have been combined with accelerometers and gyroscopes to improve the performance [37]. However, these systems are bulky, uncomfortable for extended use, and interfere with worker performance [38]. Consequently, developing wearable platforms for unobtrusive accurate continuous real-time monitoring of the trunk motion has been an active focus of research studies in the past years. The proposed platform should be unobtrusive and accurate, so it can be used reliably for prolonged periods in different professions.

Considering these requirements for the wearable platform, two different prominent types of sensors have been investigated as the possible solutions:

- **Inertial-based motion tracking**
- **Strain-based motion tracking**

The integration of these sensors has become easy and unobtrusive due to the recent advances in their underlying technology. They can be implemented as part of the cloth and create a wearable motion tracking platform that is seamlessly combined with the users' normal daily clothing. This is a great advantage that makes the application of these sensors unobtrusive for the user. The development and improvement of these systems have therefore been a compelling topic of research. Inertial-based motion tracking is mainly performed using acceleration and angular velocity information in combination with the magnetic field measurements; while in the strain-based approach, different sensors such as capacitive strain sensors, strain gauges, printed piezoresistive strain sensors, and fiber piezoresistive sensors have been used to measure the strain pattern change in the fabric. This change can then be correlated with the desirable kinematic angles of the body that induces the change. Besides these two common types of sensors, there are other types that have limitedly been investigated:

- **Fiber-optic Sensors**: Fiber-optic sensors are bending sensors that measure the density of light passing through the fiber which changes proportionally with respect to the bending angle and can be used for measuring the angle [31, 39].

- **Inductive-based sensors**: An additional type of sensor is the inductive-based sensor. Similar to the fiber-optic based sensors, this sensor relies on the amount of change of inductance induced in the sensor because of the body posture change [40].

- **Strain-gauge Sensors**: Other solutions have included more obtrusive devices that attached several strain gauge sensors to the user's skin [41, 42, 43]. In these applications of the sensors, the shifting between the sensor and the user's skin is minimized and the results of motion tracking is improved. However, the application of these sensors are limited to the clinical environment where clinicians are available for attaching and detaching the sensors to the specific areas on the user's skin.

- **Other Sensors**: Air-filled tubes and dosimeters are other types of sensors which act as pressure sensors and capacitive-based sensors respectively and have been used for joint angle measurement [44, 45].

Among the two common types of sensors, the former inertial-based one has been well studied and different aspects of employing this type of sensor have been investigated in several studies [3, 46, 47]. The application of this sensor has been shown to have limitations that hinder its widespread use in all environments. For the later strain-based approach, there have been fewer studies focused on the development of this approach [47]. However, one significant aspect of using this type of sensor is its fabric integration method. Printing the sensor on the fabric has been the earliest and most simple integration of piezoresistive sensors into the fabric [48, 49]. More recently, piezoresistive sensors have been produced in a fiber shape with diameters close to those of the regular threads [50, 51]. This integration is an excellent advantage of these sensors, which allows the seamless integration of the sensor into the fabric structure by replacing the regular thread with the fiber sensor. Mokhlespour et al. showed that users prefer a sensor integrated shirt as their activity monitoring platform as such a system was rated superior to a whole-body IMU-based motion tracking system in several aspects of usability [52]. However, these sensors also suffer from limitations such as nonlinearity, hysteresis, and long transient time between different modes.

Considering the advantages and disadvantages of the two prominent wearable motion tracking sensors, the motivation for this thesis is to develop a wearable motion tracking device that combines the two sensor types in a manner that compensates the drawbacks of each type. The developed system should have the advantage of sensors being intrinsically integrated into the clothing and also benefit from the kinematic information that IMU sensors can provide for motion tracking.

1.2 Research Objectives

As mentioned in the previous section, lower back injury risk assessment is a multifactorial problem which quantitative physical exposure measurement has been recommended as one of the informative factors for assessing the risk of injury. Existing reliable motion capture systems can not be used in the workplace environment for measuring this factor. A wearable platform capable of measuring the trunk kinematic information indoor and outdoor would therefore be beneficial to both the workers and administrators for defining useful interventions in the workplace to decrease or stop the LBP occurrence. This system should provide unobtrusive accurate continuous real-time monitoring of the trunk motion for an extended period. IMUs and fiber-strain sensors have been the two promising solutions for developing such a wearable system. Although the application, performance, data processing algorithms, limitations, and advantages of using IMUs have been well studied, the application of fiber-strain sensors for monitoring 3-dimensional complex movements of the trunk has yet to be evaluated. As a result, preliminary developing and testing of a wearable system using fiber strain sensors for monitoring trunk movements was one of the objectives of this thesis. Besides, it was hypothesized that since both IMU-based and strain-based systems have intrinsic limitations in terms of their capabilities for tracking movement, combining the two approaches in one platform and then fusing the data from the two types of sensors together might improve the total performance of the system. As a result, the objectives of this thesis are listed as follows:

Objective 1. Design and development of a wearable system using fiber strain sensors with seamless integration of the sensors into the textile and investigation of its performance in tracking 3-dimensional movements of the trunk.

Objective 2. Improving the performance of wearable motion tracking by developing an algorithm for fusing the inertial-based and strain-based data in one platform in a way that the two types of sensors compensate for each other drawbacks. The developed algorithm should not be restrained to the trunk motion tracking, and hence, it should be designed in such a way that could be implemented for all body joints. As a result, no joint kinematic constraints should be employed for improving the estimation.

Figure 1.1 shows the scope of this work. For the data fusion algorithm, this work focuses only on strain sensor and gyroscope data fusion where accelerometer and magnetometer data are neglected. Although the last two sensors data suffer from dynamic noises, they can be integrated into the developed algorithm so that the performance of the algorithm would improve. This is out of the scope of this thesis and can be followed as the future work. In an attempt to achieve these objectives, a study with 12 participants was conducted to investigate the performance of both the developed system and the data fusion algorithm.

1.3 Scientific Contributions

The conducted research throughout this thesis contributes to the advancement of wearable motion tracking by developing novel wearable devices and intelligent algorithms for analyzing the wearable sensors' data. Firstly, a novel wearable device employing a thread-like strain sensor was designed and prototyped. The device is capable of measuring the 3-dimensional relative angles of the trunk with respect to the pelvis. Secondly, the advantages and limitations of strain sensors in wearable motion tracking were identified. Thirdly, a novel motion tracking platform was introduced in this thesis. Despite the traditional approaches in the literature, the platform combines properties of both inertial-based and strain-based wearable sensors to eliminate each sensor's drawbacks which is an approach unlike anything currently in the literature. The essential component of this platform is an original data fusion algo-

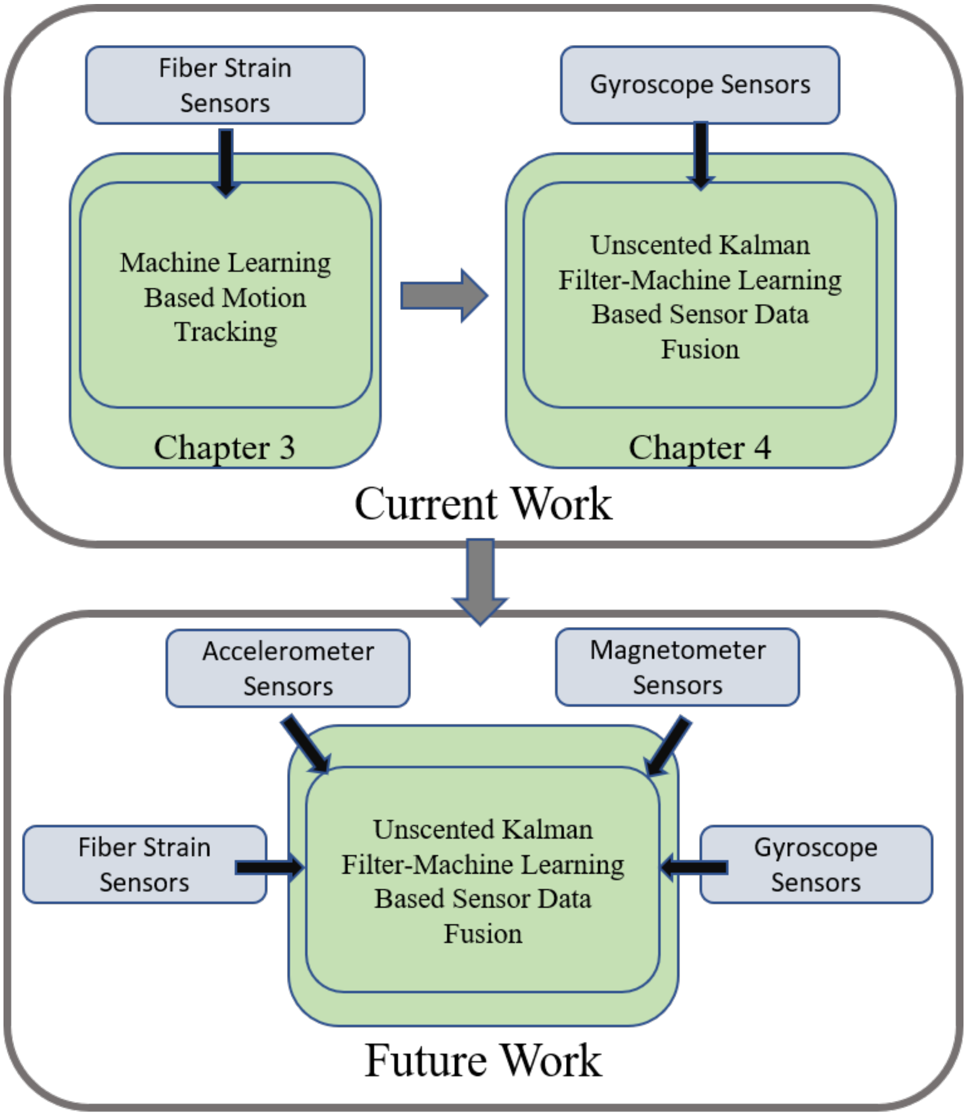

Figure 1.1: The thesis scope and the direction of the future work

rithm, which was designed to interpret the sensors' data. The results of this research led to the following academic journal publications:

- A. Rezaei, T.J. Cuthbert, M. Gholami, C. Menon, "Application-Based Production and Testing of a Core-Sheath Fiber Strain Sensor for Wearable Electronics: Feasibility Study of Using the Sensors in Measuring Tri-Axial Trunk Motion Angles", Sensors, vol. 19, no. 19, p. 4288, 2019.
- A. Rezaei, M. Khoshnam, C. Menon, "Towards User-friendly Wearable Platforms for Monitoring Unconstrained Indoor and Outdoor Activities", article in preparation.

1.4 Outline

The body of this thesis is organized as the following chapters:

Chapter 3. In this chapter, the design of a smart garment using fiber core-sheath strain sensors for monitoring 3-dimensional movements of the trunk is described, and a machine learning algorithm is developed to use the strain sensors signals for estimation the trunk Euler angles. The results of a study with 12 participants performing a set of exhaustive trunk movements while wearing the developed smart garment are presented in the chapter.

Chapter 4. This chapter describes the development of a novel data fusion filter employing unscented Kalman filter and machine learning to fuse the strain sensor and gyroscope sensor data in one single platform for compensating the drawbacks of each sensor and improving the overall performance of wearable motion tracking. As a case study, the same data set that was used in the previous chapter is used in this chapter to investigate the performance of the proposed data fusion technique and compare its estimation of the trunk motion with the machine learning regressor algorithm developed in the previous chapter.

Chapter 5. This chapter concludes the thesis by discussing how the objectives of the thesis were achieved.

Chapter 2

Background

The material of this chapter is excerpted, modified, and reproduced with permission from the following papers that I co-authored:

- A. Rezaei, T.J. Cuthbert, M. Gholami, C. Menon, "Application-Based Production and Testing of a Core-Sheath Fiber Strain Sensor for Wearable Electronics: Feasibility Study of Using the Sensors in Measuring Tri-Axial Trunk Motion Angles", Sensors, vol. 19, no. 19, p. 4288, 2019.
- A. Rezaei, M. Khoshnam, C. Menon, "Towards User-friendly Wearable Platforms for Monitoring Unconstrained Indoor and Outdoor Activities", article in preparation.

Sections of this chapter have been adapted from the above papers to fit the scope and formatting of the thesis.

2.1 Inertial-Based Motion Tracking

Inertial-based motion tracking is performed employing the kinematic information measured by inertial measurement units (IMU). IMU sensors are microelectromechanical(MEMS) sensors consisting of an accelerometer, gyroscope, and magnetometer measuring linear acceleration, angular velocity, and magnetic field strength, respectively. These sensors can capture the orientation of the sensor with respect to the earth-fixed reference coordinate system [53]. IMU sensors are of great interest in wearable motion tracking because they are lightweight, inexpensive, miniaturized, enduring(limited power consumption), and self-contained(they can operate without the need for any external sources). They have consequently been used in several different applications including health, wellness, and safety monitoring [14], gait analysis in clinical settings [54], human activity recognition [55], several medical applications of wearable motion tracking such as stabilometry, instrumented clinical tests, and tremor assessment [56]. Assuming that the physical characteristics of the MEMS sensors inside an IMU are known, the accuracy of the estimated orientation of the IMU highly depends on the algorithm exploited to fuse the information of these sensors. A significant concentration of research has therefore been on developing these filters [57].

The sensors included inside an inertial measurement unit have complementary attributes that can be used in a filtering algorithm to compensate for each sensor's drawbacks. The primary orientation estimation in IMU is conducted using the integration of angular velocity measured from the triad gyroscope sensor from a known initial orientation. This integration will lead to a considerable drift amount over a short time, even in a static posture of the sensor with no movement because of the inherent gyroscope problem: low-frequency gyro bias. If this bias value can be compensated, gyro sensor data integration can estimate the correct orientation with high accuracy even in highly dynamic movements. On the other hand, an accelerometer sensor can provide an accurate estimation in a static posture, but its accuracy drops down in dynamic movements where the linear acceleration of the body is added to the gravity acceleration measured by the sensor. As the different components of acceleration are indistinguishable for the sensor, the estimated orientation is not accurate, and the accelerometer estimation is hence only accurate in static or slowly moving objects. Another drawback of the accelerometer sensor is that it can only measure the roll and pitch Euler angles, as it uses the gravity acceleration vector as the reference. This problem necessitates the utilization of a magnetometer sensor to estimate the heading angle. This sensor has a similar problem in measuring the earth's magnetic field. When there is no ferromagnetic object close to the sensor, the magnetometer is accurate in estimating the heading angle. However, in environments where ferromagnetic objects are available, which is mostly indoor heading estimation, the accuracy of the estimation is prone to collapse. Consequently, several different filtering approaches have been introduced to overcome every single sensor's disadvantages and provide an accurate overall orientation estimation.

2.1.1 Sensor Data Fusion Algorithms

Sensor data Fusion for estimating an optimal orientation has a long history, particularly for guidance and control. Over time, three main approaches have been developed: deterministic (least square) approaches, complementary filtering algorithm (frequency-based method), and Kalman filtering [57, 58]. Among the three methods, Kalman filtering is a powerful technique for combining multisensory data. As it is mentioned in [59, p.75], Kalman filtering is "perhaps the perfect tool for elegantly combining multisensory fusion, filtering, and motion prediction in a single fast and accurate framework." The focus of this thesis is therefore on implementing a Kalman filtering approach for sensor data fusion.

Kalman Filtering

Kalman filtering approach is a solution for the general problem of state estimation when direct measurement of the system states is not possible. As formulated in [60], the state space modeling of a system in the discrete-time domain can be formulated as follows

$$\boldsymbol{x}(t_{k+1}) = f(\boldsymbol{x}(t_k), \boldsymbol{v}(t_k)) \tag{2.1a}$$

$$\boldsymbol{y}(t_k) = h(\boldsymbol{x}(t_k), \boldsymbol{n}(t_k)) \tag{2.1b}$$

in which vector $\boldsymbol{x}(t_k)$ is the state vector and vector $\boldsymbol{y}(t_k)$ is the measurement vector of the system, the function $f(\boldsymbol{x}(t_k), \boldsymbol{v}(t_k))$ is the process model that projects the previous time step state vector to the current state, and $h(\boldsymbol{x}(t_k), \boldsymbol{n}(t_k))$ is the measurement function which maps the state vector to the measurement vector. Both these functions can be nonlinear and time-variant. Considering they are both known, the exact value of the state vector can not be calculated due to the noise vectors included in this formulation. The vectors $\boldsymbol{v}(t_k)$ and $\boldsymbol{n}(t_k)$ are the process and measurement noise vectors, respectively. They are present to account for all the disturbances and mismodelling that exist in the system. From the practical point of view, the vector $\boldsymbol{x}$ is the unobserved vector which is immeasurable, and the vector $\boldsymbol{y}$ is the only observed signal in the system. Having this formulation, the problem of state estimation can be stated as: knowing the prior estimation of the state vector at time t_k as $\boldsymbol{x}(t_k)$ and the measurements of the system at time t_{k+1} as $\boldsymbol{y}(t_{k+1})$, it is intended to estimate the value of the state vector $\boldsymbol{x}_{k+1}$. To solve this problem, it is assumed that the noise vectors are white discrete noises with known probability density functions (PDF), and are statistically independent. The initial state vector is assumed to be known with known PDF at the initialization of the filter [57].

The original Kalman filtering approach introduced in [61] was for a linear system. In the case of a linear system, the system model will be simplified to

$$\boldsymbol{x}(t_{k+1}) = \boldsymbol{F}\boldsymbol{x}(t_k) + \boldsymbol{v}(t_k) \tag{2.2a}$$

$$\boldsymbol{y}(t_k) = \boldsymbol{H}\boldsymbol{x}(t_k) + \boldsymbol{n}(t_k) \tag{2.2b}$$

The Kalman filtering suggests a recursive state estimation solution for $\boldsymbol{x}(t_{k+1})$ as expressed as follows [62]

$$\hat{\boldsymbol{x}}(t_{k+1}) = (prediction\ of\ \boldsymbol{x}(t_{k+1})) + \mathcal{K}(t_{k+1})[\boldsymbol{y}(t_{k+1}) - (prediction\ of\ \boldsymbol{y}(t_{k+1}))] \tag{2.3a}$$

$$\hat{\boldsymbol{x}}(t_{k+1}) = \hat{\boldsymbol{x}}^-(t_{k+1}) + \mathcal{K}(t_{k+1})[\boldsymbol{y}(t_{k+1}) - \boldsymbol{y}^-(t_{k+1})] \tag{2.3b}$$

$\hat{\boldsymbol{x}}(t_{k+1})$ show the estimated value of $\boldsymbol{x}(t_{k+1})$. $\hat{\boldsymbol{x}}^-(t_{k+1})$ and $\boldsymbol{y}^-(t_{k+1})$ are called *a priori* estimate and are the predictions of the state and measurement calculated using the system's dynamic model (2.2) and the previous time step estimation of states ($\hat{\boldsymbol{x}}(t_k)$). This recursive filter is based on defining the $\mathcal{K}(t_{k+1})$ to find the optimal minimum mean squared error for $\boldsymbol{x}(t_{k+1})$ assuming that $\boldsymbol{y}(t_{k+1})$ and $\hat{\boldsymbol{x}}(t_k)$ are Gaussian random variables. This is a principal assumption for Kalman filter, since if the variables are Gauassian, they can be characterized using only their mean vector and covariance matrix. As mentioned before, the additive noises in 2.2 are assumed to be independent zero-mean white Gaussian with known covariance matrices $\boldsymbol{Q}$ and $\boldsymbol{R}$ which can be time-variant. The Kalman filter process is therefore as follows [57]:

1. **Initialization:** $\hat{\boldsymbol{x}}(t_0)$ and the initial covariance matrix of the state vector denoted as $\hat{\boldsymbol{P}}(t_0)$ should be known. A small value can be selected for $\hat{\boldsymbol{P}}(t_0)$ for initialization of the filter as it can be tuned to minimize the filter's divergence time, but an accurate estimation of the state vector is necessary for the correct performance of the filter.

2. **Time Update:** In this step, *a priori* estimate of the state vector and its covariance matrix are calculated.

$$\hat{\boldsymbol{x}}^{-}(t_{k+1}) = \boldsymbol{F}(t_k)\hat{\boldsymbol{x}}(t_k) \tag{2.4a}$$

$$\hat{\boldsymbol{P}}^{-}(t_{k+1}) = \boldsymbol{F}(t_k)\hat{\boldsymbol{P}}(t_k)\boldsymbol{F}^T(t_k) + \boldsymbol{Q}(t_k) \tag{2.4b}$$

3. **Measurement Update:** In this step, the measurement time update ($\hat{\boldsymbol{y}}^{-}(t_{k+1})$) and its difference with the measured value from sensors($\boldsymbol{y}(t_{k+1})$) which is denoted as innovation ($\boldsymbol{y}(t_{k+1}) - \hat{\boldsymbol{y}}^{-}(t_{k+1})$), and the innovation covariance matrix are calculated:

$$\hat{\boldsymbol{y}}^{-}(t_{k+1}) = \boldsymbol{H}(t_{k+1})\hat{\boldsymbol{x}}^{-}(t_{k+1}) \tag{2.5a}$$

$$\boldsymbol{w}(t_{k+1}) = \boldsymbol{y}(t_{k+1}) - \hat{\boldsymbol{y}}^{-}(t_{k+1}) \tag{2.5b}$$

$$\hat{\boldsymbol{S}}(t_{k+1}) = \boldsymbol{H}(t_{k+1})\hat{\boldsymbol{P}}^{-}(t_{k+1})\boldsymbol{H}^T(t_{k+1}) + \boldsymbol{R}(t_{k+1}) \tag{2.5c}$$

4. **State Correction:** The last step of the filter is correcting *a priori* estimate of the state vector by combining *a priori* estimate with the innovation using Kalman gain and calculating *a posteriori* estimate of the state vector (as it is shown in 2.3):

$$\mathcal{K}(t_{k+1}) = \hat{\boldsymbol{P}}^{-}(t_{k+1})\boldsymbol{H}^T(t_{k+1})\hat{\boldsymbol{S}}^{-1}(t_{k+1}) \tag{2.6a}$$

$$\hat{\boldsymbol{x}}(t_{k+1}) = \hat{\boldsymbol{x}}^{-}(t_{k+1}) + \mathcal{K}(t_{k+1})\boldsymbol{w}(t_{k+1}) \tag{2.6b}$$

$$\hat{\boldsymbol{P}}(t_{k+1}) = \hat{\boldsymbol{P}}^{-}(t_{k+1}) - \mathcal{K}(t_{k+1})\boldsymbol{H}(t_{k+1})\hat{\boldsymbol{P}}^{-}(t_{k+1}) \tag{2.6c}$$

The preceding process is the Kalman filter process for a linear system. In practice, most of the systems have a nonlinear state-space model. Consequently, several different versions of the Kalman filter have been developed to overcome this problem. Extended Kalman filter (EKF), Unscented Kalman filter(UKF), and particle filters are some of these filters. The most prevalent version is the EKF, which is an extension of the Kalman filter using linearization of the model using Taylor's series expansion. Considering equation 2.1 that the system has n states and m output, then using the Jacobian matrix, the linearized state-space model of the system is

$$\boldsymbol{F}(t_k) = \begin{bmatrix} \frac{\partial f_1(\boldsymbol{x}(t_k))}{\partial x_1} & \cdots & \frac{\partial f_1(\boldsymbol{x}(t_k))}{\partial x_n} \\ \vdots & \ddots & \vdots \\ \frac{\partial f_n(\boldsymbol{x}(t_k))}{\partial x_1} & \cdots & \frac{\partial f_n(\boldsymbol{x}(t_k))}{\partial x_n} \end{bmatrix} \tag{2.7a}$$

$$\boldsymbol{H}(t_k) = \begin{bmatrix} \frac{\partial h_1(\boldsymbol{x}(t_k))}{\partial x_1} & \cdots & \frac{\partial h_1(\boldsymbol{x}(t_k))}{\partial x_n} \\ \vdots & \ddots & \vdots \\ \frac{\partial h_m(\boldsymbol{x}(t_k))}{\partial x_1} & \cdots & \frac{\partial h_m(\boldsymbol{x}(t_k))}{\partial x_n} \end{bmatrix} \tag{2.7b}$$

At each step of the filter, the preceding Jacobian matrices are calculated using *a posteriori* estimate of the last step of the filter to calculate *a priori* estimate of the current step. This process increases the required computational power. Also, EKF accuracy degrades in points where there is a high nonlinearity, and the Jacobian matrix is not a good linearized estimate of the real function. As mentioned in [62], "These approximations, however, can introduce large errors in the true posterior mean and covariance of the transformed (Gaussian) random variable, which may lead to sub-optimal performance and sometimes divergence of the filter." These limitations lead to employing other versions of the Kalman filter in which the linearization problem has been solved in different approaches.

In this work, the Unscented Kalman filter(UKF) was used as the data fusion method. While Extended Kalman Filter(EKF) relies on Jacobian matrix calculation for linearization, UKF employs unscented transformation to calculate the mean and covariance matrix of a Gaussian statistical variable when it undergoes through a nonlinear function. This method preserves the statistical information accuracy and outperforms the EKF when the nonlinear characteristics are strong. UKF provides a good estimation accuracy with a computational complexity comparable with the EKF and other nonlinear filters. The details of this filter are provided in Chapter 4.

In the context of using Kalman filtering for orientation estimation by employing IMU sensors, different state-space models have been employed [57, 63]. The typical approach is to use the gyroscope data integration in the process model and the orientation calculated from the accelerometer and magnetometer data in the measurement model of the filter. This accelerometer/magnetometer based orientation is with respect to the inertial ground frame, and several algorithms have been used for its calculation [64, 65]. Overall, roll and pitch Euler angles estimations are provided from accelerometer and yaw, or heading angle is provided from magnetometer data. In this work, accelerometer and magnetometer data are discarded, and instead, it is hypothesized that strain sensor data can provide the required estimation of the angle for Kalman filter. The details are discussed in Chapter 4.

2.1.2 Inertial-Based Motion Tracking Limitations

Several IMU units can be used together to form a wearable inertial motion capture (IMC) system. Recently, IMC systems have been used in several kinematic information measurement applications, tracking the lower extremities [66], spine [67, 68], and trunk [69]. However, important performance limitations of the IMCs have been reported [46, 70]. The IMC performance accuracy was shown to decrease significantly by the movement characteristics (movement complexity, range, speed, and period) [46, 53, 70, 71, 72, 73]. Fast complex movements over long periods have higher errors compared to short, simple tasks [70, 74]. Besides, magnetometers are extremely sensitive to the ferromagnetic environmental disturbances and cause a considerable amount of error in IMU heading estimation [75, 76]. These limitations restrict the prolonged application of IMCs for workplaces with ferromagnetic objects present in the environment.

Consequently, as ferromagnetic objects are always available indoor, this limitation has hindered the widespread application of IMCs for indoor motion tracking. In this thesis, accelerometer and magnetometer sensors were replaced with strain sensors, so the flaws that are introduced to the system because of using these sensors would be eliminated. This method is a novel approach of wearable motion tracking which limited studies have studied its feasibility. The next section describes the previous works focus on fusing IMU and strain sensor data.

2.2 Strain-Based Motion Tracking

Considering the mentioned limitations of IMC, the application of smart textiles has been investigated as a substitute for IMC systems. Smart sensing textiles have sensors integrated into the textile and have shown great potential for measuring human joint angles [50, 77]. In this application, the strain sensor can be integrated into the textile at specific positions on the garment that strain when movement occurs [78]. The application of these systems has been applied for task classification, speech recognition, gait analysis, and planar movement angle measurement [50, 77, 78, 79, 80, 81].

2.2.1 Machine Learning

Various algorithms have been employed for strain sensors signal processing. Among them, machine learning algorithms are the most prevalent for this purpose. Support Vector Machines(SVMs), Neural Network, and Random Forest are frequently used for classification and regression when processing strain sensor data. While random forest decides about the samples by averaging the decision of a set of trained decision trees [82], support vector machines use some specific data points as support vectors, and use kernel functions for mapping the data points to a space with higher dimension to make the data linearly separable [83]. Neural Networks are comprised of a set of layers, where each layer has a predefined number of neurons or nodes. This algorithm works based on back-propagating the error in each step of the training to find the weight and bias parameters which are then used for connecting the neurons to each other [84].

Comparing these three algorithms, random forest has a superior performance in angle estimation and task classification applications using smart textiles and strain sensors [50, 77, 85, 86]. Therefore, random forest regressor algorithm was selected for analyzing the data in this work. Random Forest is an ensemble of decision trees each trained on a boot-strap sample of training data. Boot-strap samples are generated by randomly selecting data points from training data with replacement (i.e., one data point might be selected several times) [87]. A decision tree is then built using each boot-strap sample, and a subset of random features is used for splitting nodes of trees. Each tree generates a prediction of the angle, and random forest then chooses the final angle estimation by a majority vote between the prediction of all trees. Compared to a single decision tree, random forest is robust to overfitting on the training data, and has a smaller generalization error [87].

2.2.2 Feature Extraction and Selection

Feature extraction is a common technique when analyzing time series data, that can improve the performance accuracy of the employed machine learning algorithm. In many applications, it is common for the number of features at each data point (depending on the size of the selected window) to be the same or bigger than all of the observed data points. This may lead to a problem called overfitting of the model during training. In these cases, dimension reduction can be used by employing feature extraction. Additionally, feature extraction can add new information to the data set that was not originally available from the observations. The challenging part of the feature extraction is selecting the best possible features. When prior knowledge of the domain is available, one can use this knowledge to extract the most relevant features. However, in many cases such as in this thesis, there is no prior knowledge of the domain available. In such cases, one possible solution is to employ a technique called automatic feature extraction. In this approach, a massive feature set derived from scientific literature is extracted from the data set. However, most of these features are not informative, and employing them decreases the accuracy. Consequently, a feature selection algorithm such as the greedy forward feature selection [88] or tree-based ranking [50] is then applied to the extracted features. The feature selection algorithm grows a subset of features by employing the training data set and by sorting the features based on their importance, choosing the most important one as the first entry of the subset. The process is continued by adding more features and is terminated when a pre-defined termination criteria is satisfied. This criteria depends on the employed feature selection algorithm. The selected subset of features then provides the input for the machine learning algorithm. This feature extraction-selection approach was conducted in chapter 3 of this thesis.

2.2.3 Strain-Based Motion Tracking Limitations

The potential of smart sensing textiles for angle measurement in simple planar movements and joints with one degree-of-freedom such as knee and fingers has been well established. The application of these sensors for such joints has shown a promising accuracy [79]; however, the feasibility of these systems for angle measurement in complex multiplanar movements has yet to be evaluated. Due to the limitations of this type of sensor, which are hysteresis, dependency on speed, drift, and nonlinearity, it is expected that the performance of the sensors would degrade as the movements become more complex. A potential solution for this problem might be the data fusion of these sensors with the typical IMU sensor for overall performance improvement.

2.3 Inertial and Strain Sensor Data Fusion

As mentioned in the previous sections, there have been two prominent approaches for wearable motion tracking, both with their specific advantages and disadvantages. As sensor data fusion improves the overall performance of the motion tracking in IMUs, adding strain sensor data can furthermore overcome the defects of IMUs. However, the study of combining the two types of sensors in one single platform has been limited in the literature. In [89], a wearable system capable of estimating the local curvature and length of the spine was developed. This system comprised a set of piezoresistive strain sensors printed on the garment and two accelerometers. The strain sensor behavior while undergoing stretch was modeled as two phases of extending and shortening. A trigger signal was required to determine the current phase of the sensor. This task was performed utilizing the tri-axial accelerometers determining the flexion-extension angle of the spine. Consequently, accelerometer sensors were used only as the trigger for choosing the governing model of the strain sensor, and no data fusion algorithm was employed. In a more recent work [90], a platform combining e-textile goniometers and tri-axial accelerometers was used for knee angle estimation. Considering the governing equation of the goniometer and the angles provided from accelerometers, a Kalman filter was designed and tested for combining the two sensors' data. This study had several limitations. First, The performance of the developed algorithm was compared against the estimation of an inertial-based motion tracking system. The proposed solution in this work was more complex than the employed reference angle measurement system by adding the goniometer sensor. Their developed algorithm was feasible only for a simple joint such as knee in which there is a robust geometrical constraint. The feasibility of this algorithm for more complex joints such as trunk and hip was not clear. The developed algorithm in this work was highly relying on the governing equation of the textile goniometer. However, if this sensor was replaced with other textile-based strain sensors such as the fiber strain sensor used in this thesis, the developed algorithm was impractical. Despite the limitations, this work demonstrates the importance of the textile-based and inertial-based data fusion for motion tracking, where the performance of the combined system was superior to the accuracy of both accelerometer or textile sensors employed separately. In another work, IMU and textile-based goniometer sensors were combined to improve the accuracy of detecting the position of the hand with respect to the sternum [91]. Data from the two sensors were employed in a bi-articular model of the shoulder, and a direct data fusion of the two types of sensors was not employed.

The previous work for fusing the two sensor types in one algorithm has been limited. In the current work, a novel data fusion technique for employing the gyroscope and strain sensor data is proposed. To avoid potential problems, this algorithm does not use the accelerometer or magnetometer for data processing. Despite the previous works, no geometrical constraints were utilized, so the application of this scheme can be expanded to all body joints.

Chapter 3

Measuring Tri-axial Trunk Motion Angles: A Feasibility Study Using Machine Learning and Wearable Core-Sheath Fiber Strain Sensors

The material of this chapter is excerpted, modified, and reproduced with permission from the following papers that I co-authored:

- A. Rezaei, T.J. Cuthbert, M. Gholami, C. Menon, "Application-Based Production and Testing of a Core-Sheath Fiber Strain Sensor for Wearable Electronics: Feasibility Study of Using the Sensors in Measuring Tri-Axial Trunk Motion Angles", Sensors, vol. 19, no. 19, p. 4288, 2019.
- A. Rezaei, M. Khoshnam, C. Menon, "Towards User-friendly Wearable Platforms for Monitoring Unconstrained Indoor and Outdoor Activities", article in preparation.

Sections of this chapter have been adapted from the above papers to fit the scope and formatting of the thesis.

3.1 introduction

In this chapter, the feasibility of using a fiber core-sheath strain sensor integrated into a garment for measuring 3-dimensional kinematic angles of the trunk relative to the pelvis in simple uniaxial and complex multiaxial movements is investigated. The design and development of this smart garment are described, and the application of a machine learning algorithm to sensor signals for angle estimation is demonstrated. The performance of this algorithm in a study with 12 participants performing simple to complex movements likely to occur in real application scenarios is then evaluated.

3.2 Materials and Methods

3.2.1 Sensor Integrated Sleeveless Shirt

A sensor-integrated sleeveless shirt was developed to measure the 3-dimensional angles of the trunk movements relative to the pelvis. The prototype was designed to be capable of measuring the trunk kinematics data in a variety of movements, including the uniaxial and multiaxial movements of the trunk. The following sections describe the elements of this design.

Fiber Core-sheath Strain Sensor

The sensing element of the shirt was a fiber core-sheath strain sensor that was developed, tested, and characterized in the Menrva Research group [51]. This sensor had a diameter of ca. 0.45mm and the potential to be fully integrated into the fabric as a stitched thread. It had a non-conductive core coated with conductive sheath. The non-conductive core was produced by melt extrusion of Hytrel 3078 (DuPont, Kingston Canada) with a Filabot EX2 extrusion system with a 0.4mm die set at a temperature of 190°C, producing 450μm filaments spooling 30cm below the die onto a clean surface. The filament was then dip-coated with a 50wt% mixture of carbon black and Hytrel 3078 in dichloromethane (5wt% Hytrel 3078 in dichloromethane) at a rate of 3.81cm/second wound onto a bobbin 1.83meters from the exit of the coating solution. The coated filaments were then dried in vacuo at 60°C for a minimum of 30 minutes. The sensors were then conditioned using a linear stage straining with a sinusoidal wave pattern from 0-40% strain 100x at a strain rate of 10%s^{-1}. This sensor had a working range up to 30% strain. To protect the sensor from shorting when exposed to conductive liquids or solids, an additional insulating sheath was applied. Figure 3.1 shows the fiber strain sensor prior(Figure 3.1a) and after(Figure 3.1b) embedding in the fabric along with its performance characteristics.

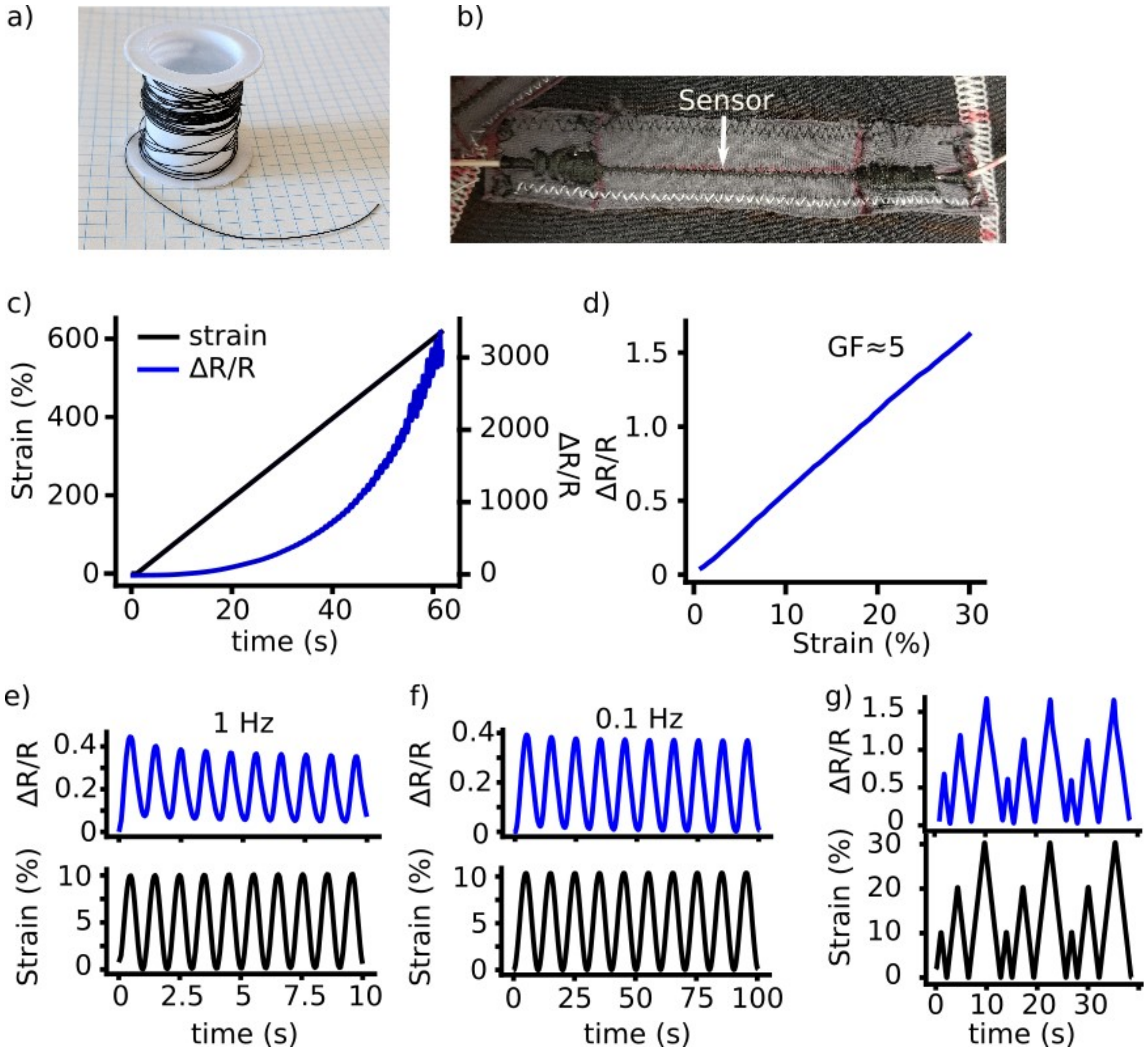

Figure 3.1: Fiber strain sensor with 450μm diameter that could be integrated into the textile by stitching or weaving. a) Fiber sensor before embedding into the textile; b) Fiber sensor after integration into the textile with stitches over the length of the sensor; c) Stack plot of strain vs. time and resistance vs. time; d) Resistance vs. strain within the working range of the sensor displaying the linearity of the resistance response (gauge factor=5); e) Sensor response at a 1Hz frequency; f) Sensor resistance change at a 0.1 Hz frequency; g) 3 consecutive trapezoid cycles at 10, 20, and 30% strain.

As it can be seen in Figure 3.1d, the sensor's resistance is correlated linearly with the applied strain and changes by a factor of 5 versus the change in length (gauge factor). Figures 3.1e and 3.1f display the sensor's resistance change in 1 Hz and 0.1 Hz and shows the sensor has a more consistent performance at lower speeds. Figure 3.1g shows the sensor's resistance change while strained consecutively to 10%, 20%, and 30% strain. This characteristic can be used to calculate the applied strain to the sensor using the change in resistance.

In Figure 3.1g, using random forest method with the sensor's resistance as input and the corresponding strain value as output, the resistance followed the strain with a normalized root mean squared error of 1.6% error. For the trunk movement angle measurement application, the same correlation between the change in the resistance value and the joint angular displacement was derived.

Sensor Placement

The working principle of this smart garment was to monitor fabric strain that occurs because of the user's motion. Mattmann et al. developed optical-based strain patterns of fabric on the trunk back side area while performing 27 distinct movements using a grid of reflective markers attached to the garment [92]. Within the patterns, there was consistent vertical strain along the length of the spine during trunk flexion-extension and lateral bending. Consmüller et al. used two strain gauge sensors strips attached to human skin on both sides of the spine, and using the information of two strips, showed the upper body motions in different anatomical planes were distinguishable [93]. Consequently, two strips of sensors, each consisting of five 6cm strain sensors were integrated on both sides of the spine, covering the lower and upper back in a garment (Figure 23.2). Each sensor strip was 6cm apart from the spine. In addition to the information that each one of these two sensor strips provided for detecting trunk flexion in forward bending, they can also be used for detecting movements in two other planes (lateral bending and rotation) by calculating the difference of the signals between the symmetrical sensors in the strips on either side of the spine. Using the strain patterns by Mattmann et al. as a starting point and conducting further empirical sensor placement tests, the placements shown in Figure 3.2 was found to provide the best strain patterns for trunk twisting and lateral bending [92]. This placement resulted in more sensitivity to rotation and lateral bending movements (as a result of more elongation of the sensors) and was isolated from the trunk flexion movement (no elongation of the sensors). In total, 18 sensors were integrated into the shirt for detecting all types of movements.

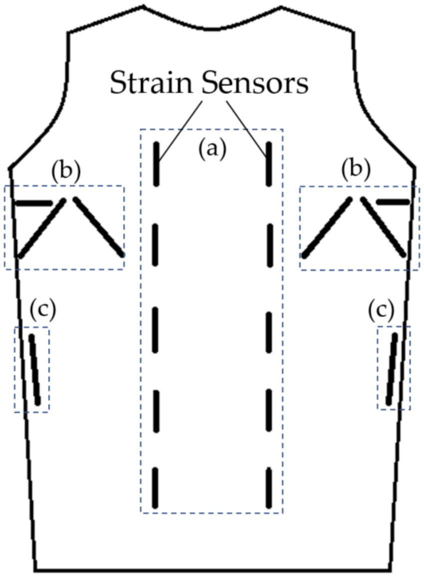

Figure 3.2: Schematic illustration of the placement of 18 strain sensors on the garment. Each short line shows one strain sensor. Two vertical strips of sensors in the box (a) provide information for flexion, rotation, and lateral bending movements, whereas sensors in boxes (b) and (c) are specifically for detecting rotation and lateral bending, respectively. These sensors are isolated from the trunk flexion movement.

Smart Sleeveless Shirt

The sensor's 450μm diameter could allow the integration into textiles by stitching or weaving. This provided the potential to fabricate smart clothing with the sensors integrated directly into the textile structure. In our prototype, we attached the sensor to fabric using stitches over the length of the sensor (Figure 3.1b). Wires were connected to the ends of the sensor using conductive ink and rubber glue. A commercially available tight-fitting sleeveless shirt for integrating the sensors was selected. Eighteen sensors were integrated into the back side of the shirt to measure the strain pattern of the fabric. Shoulder and arm movements cause significant unwanted strain pattern change in the fabric of sleeved shirts [92, 94]. A sleeveless shirt Was intentionally chosen to reduce this unwanted change and isolate the strain pattern associated with trunk motions.

One crucial challenge of using strain-based clothing for trunk motion detection is the upward shifting of the garment at the waistline during movement. It has been shown previously that a 3 cm shift decreases the accuracy by more than 20% in an upper-body task

Figure 3.3: The two-piece smart prototype with sensor integrated sleeveless shirt and shorts. Sensors were integrated on the back side of the shirt into the textile. (a) A participant wearing the prototype. Shirt was anchored to shorts with Velcro patches to minimize the upward shift at the waistline; (b) Two reflective marker sets attached to participant C7 and S1 vertebras for generating reference kinematic angles using motion capture system.

classification problem using a smart catsuit [92], and care should be taken to minimize any waistline shift. The use of a leotard [95] or catsuit [78], or straps [79, 96] has been used to minimize this slippage. In an attempt to anchor the shirt to minimize this slippage, a two-piece prototype (shirts and shorts) was used that allowed anchoring of the shirt to the shorts with Velcro patches. This allowed the comfortable extended use of this system under normal clothing without the use of a leotard/catsuit with minimal slippage. Figure 3.3a shows the two-piece prototype.

3.2.2 Experimental Setup

A voltage divider was used for reading the change of resistance in sensors. Each sensor was connected to a resistor to form a voltage divider with a 5V voltage source. The resistor value was selected to match the base resistance of the sensor, ca. $10k\Omega$. Two data acquisition boards (Models NI BNC-2110 and NI BNC-2111, National Instruments, Austin, TX, USA) were used for reading voltage signals of all sensors. MATLAB R2017b (The MathWorks, Inc., Natick, MA, USA) was used for data collection.

For collecting the trunk kinematics data, A Vicon motion capture system (Vicon, Oxford, UK) was used. This system consisted of six infrared motion tracking cameras. Two sets of reflective markers, each with five markers (8 mm diameter) were used to track objects. These two marker sets were mounted on the participants' spinal C7 and S1 vertebras. The markers' cartesian coordinates information was used to generate the movements' kinematic data. Figure 3b shows the tracker markers attached to a participant's back. A synchronization signal from motion tracking system was used for synching the sensors and motion capture data. Data from all components were recorded at a frequency of 100Hz.

3.2.3 Participants

To evaluate the performance of the prototype, 12 healthy male individuals were recruited between the ages of 25 and 35. The experimental protocol was approved by the Office of Research Ethics at Simon Fraser University. Prior to any data collection, written informed consent was obtained from all participants. Table 3.1 provides the characteristics of the participants.

Table 3.1: Participants characteristics

	Participant
Age(years)	28(3.3)
Height(cm)	177(7.6)
Weight(kg)	75(9.8)

3.2.4 Study Protocol

The data collection for each participant lasted for 1.25 hours, including the preparation time. The shirt was anchored to the short at the waist level using three Velcro patches. The positioning of the short was adjusted based on the participant's feedback to ensure the participants were comfortable during data collection. The participants were then asked to stand upright on a flat floor with feet shoulder-width apart and arms hanging to the sides of their body for the duration of the experiment. A 10s trial was then recorded in this static posture. This trial was used for the standardization of all sensor data in the next trials.

The study protocol included four conditions of uniaxial movements and four conditions of multiaxial movements. Table 3.2 provides a list of the movements' conditions. Since people's common everyday movements include both uniaxial and multiaxial movements, an exhaustive combination of the uniaxial movements was selected as part of the study protocol. For each movement condition, participants were asked to perform the movement in 3 separate trials, each of them with the self-selected speeds of slow, moderate, and fast. In each trial, the movement was repeated 10 times. The range of motion of each repetition was self-selected by the participant, with a limit of maximum comfortable angle. This resulted in movements with different ranges of motion within each trial. For the random combination movement condition, participants were asked to perform random combinations of all the movements in a random order, with random ranges of motion for 60s. During all trials, the participants were asked to perform the movements naturally and keep the self-selected speed constant.

3.2.5 Data Analysis

Reference Angle Measurement

Trunk reference kinematics angles (Eulerian roll, pitch, and yaw angles) were calculated using the mocap data. Two marker sets were attached to C7 and S1 vertebras. Mocap provides the cartesian coordinates of the markers in each marker set. In each marker set, local unit vectors X and Y were constructed using the coordinates data and unit vector Z using the cross product of X and Y unit vectors (Figure 3.3b). The relative rotation matrix

Table 3.2: Study protocol movement conditions and types

Trial Number	Movement Condition	Movement Type
1-3	Rotation(R)	Uniaxial
4-6	Lateral Bending(LB)	Uniaxial
7-9	Flexion(F)	Uniaxial
10-12	Slouching(S)	Uniaxial
13-15	Flexion + Lateral Bending(FLB)	Multiaxial
16-18	Flexion + Rotation(FR)	Multiaxial
19-21	Lateral Bending + Rotation(LBR)	Multiaxial
22-24	Random Movement(RM)	Multiaxial

between C7 and S1 then was computed:

$$
{}^{C_7}_{S_1}R = \begin{bmatrix} X_{C_7}.X_{S_1} & X_{C_7}.Y_{S_1} & X_{C_7}.Z_{S_1} \\ Y_{C_7}.X_{S_1} & Y_{C_7}.Y_{S_1} & Y_{C_7}.Z_{S_1} \\ Z_{C_7}.X_{S_1} & Z_{C_7}.Y_{S_1} & Z_{C_7}.Z_{S_1} \end{bmatrix} \tag{3.1}
$$

in which ${}^{C_7}_{S_1}R$ denotes the relative rotation matrix, and X_{C_7}, Y_{C_7}, Z_{C_7} and X_{S_1}, Y_{S_1}, Z_{S_1} are the C_7 and S_1 coordinate frame unit vectors, respectively. Each cell of this matrix was the inner product of the two vectors. Using this rotation matrix and the Z-Y-X Euler angles convention, Euler angles Ψ (roll, flexion angle), Θ (pitch, rotation angle), and Φ (yaw, lateral bending) around the lateral-medial, superior-inferior and anterior-posterior axes were calculated. The relative orientation of trunk (C7) with respect to pelvis (S1) was expressed using these three angles.

Accuracy of Reference Angle Measurement

The literature shows that 1 mm is considered standard for the Vicon motion capture system error in calculating the position of each reflective marker [97]. Suppose that there are two markers A and B, the absolute error for the position of each marker can be shown as follows:

$$A = (a_1 \pm 1)\hat{\imath} + (a_2 \pm 1)\hat{\jmath} + (a_3 \pm 1)\hat{k} \tag{3.2a}$$

$$B = (b_1 \pm 1)\hat{\imath} + (b_2 \pm 1)\hat{\jmath} + (b_3 \pm 1)\hat{k} \tag{3.2b}$$

The vector $\vec{\boldsymbol{X}}$ between the two markers can then be expressed as follows:

$$\vec{\boldsymbol{X}} = (a_1 - b_1 \pm 2)\hat{\imath} + (a_2 - b_2 \pm 2)\hat{\jmath} + (a_3 - b_3 \pm 2)\hat{k} = (x_1 \pm 2)\hat{\imath} + (x_2 \pm 2)\hat{\jmath} + (x_3 \pm 2)\hat{k} \tag{3.3}$$

Therefore, each component of vectors X_{C_7}, Y_{C_7}, Z_{C_7}, X_{S_1}, Y_{S_1}, and Z_{S_1} has a maximum of 2 mm error. The angles Ψ, Θ, and Φ are calculated using the equation 3.1 and following formulas:

$$\Psi = \arctan\left(\frac{Z_{C_7}.Y_{S_1}}{Z_{C_7}.Z_{S_1}}\right) \tag{3.4a}$$

$$\Theta = -\arcsin(Z_{C_7}.X_{S_1}) \tag{3.4b}$$

$$\Phi = \arctan\left(\frac{Y_{C_7}.X_{S_1}}{X_{C_7}.X_{S_1}}\right) \tag{3.4c}$$

Suppose equations $\theta_1 = \arctan(\frac{a}{b})$ and $\theta_2 = \arcsin(a)$, in which a and b have an absolute errors of $\Delta(a)$ and $\Delta(b)$, respectively. The absolute errors of θ_1 and θ_2 can then be calculated as:

$$\Delta(\theta_1) = \frac{b}{a^2 + b^2}\Delta(a) + \frac{a}{a^2 + b^2}\Delta(b) \tag{3.5a}$$

$$\Delta(\theta_2) = \frac{\Delta(a)}{\sqrt{1 - a^2}} \tag{3.5b}$$

Considering equations 3.4 and 3.5, the errors in calculating angles Ψ, Θ, and Φ can be formulated as:

$$\Delta(\Psi) = \frac{(Z_{C_7}.Z_{S_1})\Delta(Z_{C_7}.Y_{S_1}) + (Z_{C_7}.Y_{S_1})\Delta(Z_{C_7}.Z_{S_1})}{(Z_{C_7}.Y_{S_1})^2 + (Z_{C_7}.Z_{S_1})^2} \tag{3.6a}$$

$$\Delta(\Theta) = \frac{\Delta(Z_{C_7}.X_{S_1})}{\sqrt{1-(Z_{C_7}.X_{S_1})^2}} \tag{3.6b}$$

$$\Delta(\Phi) = \frac{(X_{C_7}.X_{S_1})\Delta(Y_{C_7}.X_{S_1}) + (Y_{C_7}.X_{S_1})\Delta(X_{C_7}.X_{S_1})}{(Y_{C_7}.X_{S_1})^2 + (X_{C_7}.X_{S_1})^2} \tag{3.6c}$$

Equation 3.6 requires the absolute error of the inner products. This error was then calculated using the equation 3.3 as follows:

$$\vec{\boldsymbol{X}}.\vec{\boldsymbol{Y}} = ((x_1 \pm 2)\hat{\imath} + (x_2 \pm 2)\hat{\jmath} + (x_3 \pm 2)\hat{k}).((y_1 \pm 2)\hat{\imath} + (y_2 \pm 2)\hat{\jmath} + (y_3 \pm 2)\hat{k}) \tag{3.7a}$$

$$= ((x_1 \pm 2)(y_1 \pm 2)) + ((x_2 \pm 2)(y_2 \pm 2)) + ((x_3 \pm 2)(y_3 \pm 2)) \tag{3.7b}$$

$$= (x_1y_1 + x_2y_2 + x_3y_3) \pm 2(x_1 + x_2 + x_3 + y_1 + y_2 + y_3 + 6) \tag{3.7c}$$

$$= (x_1y_1 + x_2y_2 + x_3y_3) \pm \Delta(\vec{\boldsymbol{X}}.\vec{\boldsymbol{Y}}) \tag{3.7d}$$

$$\Delta(\vec{\boldsymbol{X}}.\vec{\boldsymbol{Y}}) = 2(x_1 + x_2 + x_3 + y_1 + y_2 + y_3 + 6) \tag{3.7e}$$

Overall, incorporating equations 3.6 and 3.7, the error of the reference relative orientation at each data point can be calculated. Following this approach, the reference error for all collected data points in the three angles was less than 2°. However, as there is no other system available that can provide a more accurate estimation of the relative orientation, this error was neglected, and the reference angles were assumed to be accurate.

Signal Processing

The voltage signals collected from strain sensors had a high-frequency noise. To remove this noise, A 10th order median filter was applied to the voltage signal of each sensor. It has been reported that a 20Hz frequency was a suitable data collection frequency for monitoring normal human activities [98], and consequently, the data voltage signals were then resampled to 20Hz.

Slight differences between the sensors' base resistance resulted in differences between the working voltage range of the sensors. Using the signal collected in the initial static trial, each sensor signal was normalized using:

$$S_i(t)_{normalized} = \frac{S_i(t) - S_{i,mean}}{S_{i,max}} \tag{3.8}$$

where $S_i(t)$ is the sensor i voltage signal at time t, $S_{i,mean}$ is the mean value of that sensor voltage in the static trial, $S_{i,max}$ is the maximum value of the signal, and $S_i(t)_{normalized}$ is the normalized value of the signal in time t. Normalization brought all the signals from different sensors in the same working range.

As the placement of the sensors on the back side of the shirt was symmetrical, the difference between the signals of each symmetrical pair of sensors placed on the left and right sides of the shirt back was added to the raw data. $(\Delta v_l - \Delta v_r)$ shows this difference, in which Δv_l and Δv_r are the left sensor signal and the corresponding symmetrical right sensor signal, respectively. In addition to this difference, the derivative of the signals was added to the raw data set. Adding these new signals provided the angle measurement algorithm with more information for detecting multiaxial movements and improved the angle estimation accuracy.

To generate the input for the angle measurement algorithm, a 1s sliding window was used over the raw data signals. The window length was determined empirically by performing a grid search over windows with length 100ms to 3s to find the best performance in estimating the angles. As described in chapter 2, a feature extraction-selection approach was then applied to the raw signal data using the 1s sliding window. The extracted features consisted of minimum, maximum, mean, variance, median, root-mean-square, sum of absolute value, mean absolute deviation, wave length, and slope sign changes. Adding more complex time and frequency domain features did not improve the performance of the random forest regressor and these features were not consequently included in the feature subset. The extracted features, along with the raw data of the window, were then used as inputs for the angle measurement algorithm.

A random forest regressor algorithm was used for the angle estimation algorithm to train and test the model. Raw data, along with the extracted features, formed the input, and the roll, pitch, and yaw angles formed the output of the random forest regressor. Python scikit-learn machine learning package was used for training and testing the estimator model [99].

Evaluation

The performance of the angle measurement machine learning algorithm was assessed by comparing the predicted angle from the algorithm with the actual reference angle measured from the motion capture system. The coefficient of determination (R^2), the root mean squared error (RMSE), and the normalized root mean squared error (NRMSE) were used as the criteria for this comparison.

Using these criteria, the performance of the machine learning algorithm was validated in an intra-subject analysis. In this evaluation approach, one separate model was trained and tested for each subject. A 3-fold cross-validation method was employed to evaluate the performance of the model. Each fold comprised all movement conditions with the same speed. Consequently, there were three folds corresponding to slow, moderate, and fast movements. In this 3-fold cross-validation approach, the model was trained using the data from two folds and tested on the remaining fold. This was repeated until all three folds were selected as the test set. The accuracy of the model was then determined by averaging the results of all three folds.

3.3 Results

For each participant, one hour trunk motion data comprised of 24 different trials was collected. Figure 3.4 shows a sample of the collected strain sensors voltage data and the corresponding principal trunk kinematics angle in uniaxial trunk flexion (Figure 3.4a), rotation (Figure 3.4b), and lateral bending (Figure 3.4c) movements. In each movement type, only the relevant sensors of that movement type were strained so that the voltage patterns were different between different movement types. The range of motion was different between different degrees of freedom ranging from 40° to 80°.

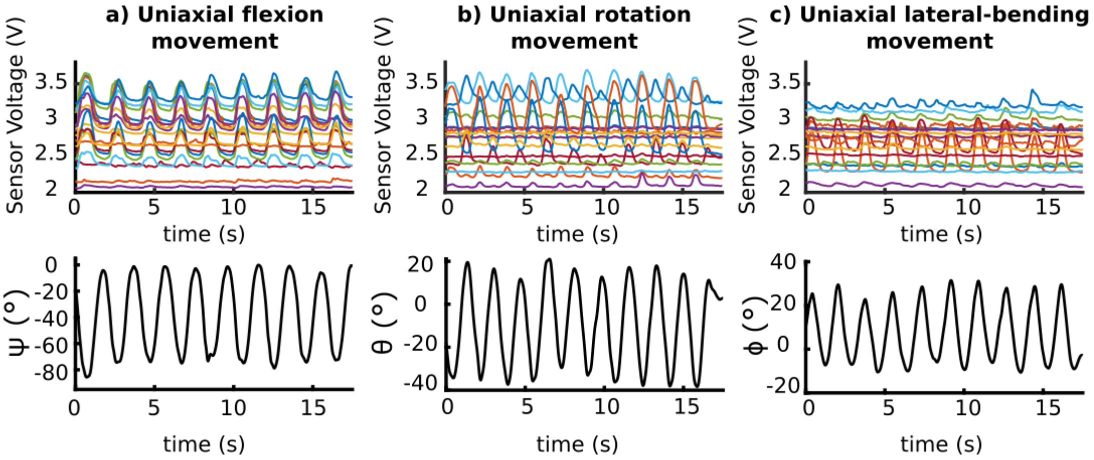

Figure 3.4: Unnormalized change of strain sensors voltage while performing three different types of movement. As a result of the specific sensor placement, voltage change depended on movement type, and in each specific movement, only sensors related to that movement were strained. (a) Uniaxial flexion movement of the trunk; (b) Uniaxial rotation movement of the trunk; (c) Uniaxial lateral bending of the trunk.

Averaged across all uniaxial and multiaxial movement conditions, random forest regressor estimated the roll angle with R^2= 0.94 ± 0.03, RMSE = 4.26°± 1.06°, and NRMSE = 5.04% ± 1.05%; the pitch angle with R^2= 0.92 ± 0.03, RMSE = 3.52°± 0.73°, and NRMSE = 4.65% ± 0.94%; and the yaw angle with R^2=0.91 ± 0.03, RMSE = 3.40°± 0.62°, and NRMSE = 5.71% ± 0.85% averaged over all participants. Table 3.3 shows the detailed results of angle estimation for all participants, with an error ranging from 2.87% to 6.47% for all 3 angles among all participants. While trunk flexion and lateral bending had errors higher than 5%, the trunk rotation angle was estimated slightly better than the two other angles with an error less than 5%.

Table 3.4 presents the detailed results of angle estimation in each movement condition among all participants. Algorithm estimated the principal angles in uniaxial movements accurately (R^2 >0.97). As the movement became more complex, the error in estimating angles increased with the maximum error happening in the random combination movement condition (NRMSE between 7% and 10%).

Table 3.3: Performance results of the algorithm in the detection of 3 angles of Ψ (flexion), Θ (rotation), and Φ (lateral bending) for each participant (P).

	Ψ			Θ			Φ		
	R^2	RMSE (deg)	NRMSE (%)	R^2	RMSE (deg)	NRMSE (%)	R^2	RMSE (deg)	NRMSE (%)
P01	0.97	2.75	3.21	0.97	2.31	2.87	0.96	2.30	3.35
P02	0.92	5.80	5.70	0.91	4.48	4.84	0.90	4.63	6.10
P03	0.96	4.07	4.52	0.90	3.84	5.57	0.94	3.97	6.20
P04	0.97	2.61	3.89	0.89	Ĺ2.45	5.90	0.91	2.80	6.47
P05	0.95	3.69	5.10	0.90	4.06	5.10	0.88	3.46	6.07
P06	0.92	3.71	5.77	0.94	2.87	4.08	0.91	2.71	6.30
P07	0.85	4.04	6.64	0.88	3.46	5.54	0.88	3.24	6.30
P08	0.91	5.35	6.31	0.92	4.29	4.98	0.88	3.44	6.10
P09	0.96	5.37	4.58	0.93	4.32	4.96	0.93	3.63	5.53
P10	0.96	4.22	4.24	0.96	3.47	3.66	0.89	3.84	5.30
P11	0.94	3.89	5.99	0.96	3.24	3.43	0.93	3.12	5.33
P12	0.96	5.59	4.54	0.93	3.57	4.87	0.91	3.70	5.52
Mean	0.94 (0.03)	4.26 (1.06)	5.04 (1.05)	0.92 (0.03)	3.52 (0.73)	4.65 (0.94)	0.91 (0.03)	3.40 (0.62)	5.71 (0.85)

Table 3.5 reports the detailed performance of the algorithm for each of the three self-selected speeds. Among the 3 angles, movements with moderate speed had the best performance with the maximum accuracy ($R^2 = 0.96$ in flexion angle) whereas fast movements had lower angle estimation accuracy ($R^2 = 0.90$ in rotation angle).

Figure 3.5 shows an exemplary comparison between the real and estimated principal angles in 3 different uniaxial movements, whereas Figure 3.6 demonstrates all 3 angles in 4 multiaxial movement conditions. Random forest regressor estimation follows the actual angle pattern in all complex movements ($R^2 > 0.82$). Flexion angle had the minimum decrease in accuracy with $R^2 = 0.85$ in the random combination movement condition.

Table 3.4: Performance results of the algorithm in the detection of 3 angles of Ψ (flexion), Θ (rotation), and Φ (lateral bending) for each participant (P).

	Ψ			Θ			Φ		
	R^2	RMSE (deg)	NRMSE (%)	R^2	RMSE (deg)	NRMSE (%)	R^2	RMSE (deg)	NRMSE (%)
R	0.94	3.23	3.91	0.97	1.66	2.41	0.94	2.45	3.73
LB	0.93	3.65	4.32	0.83	3.60	3.07	0.98	1.94	2.84
F	0.97	3.08	3.49	0.85	4.16	3.52	0.87	2.13	4.34
S	0.95	2.39	3.39	0.93	1.17	2.85	0.94	2.12	4.26
FLB	0.87	4.27	8.78	0.89	4.08	4.85	0.92	3.12	6.04
FR	0.92	4.60	7.10	0.87	4.36	6.83	0.82	3.02	8.03
LBR	0.92	4.29	7.25	0.86	4.26	5.83	0.97	3.38	5.42
RM	0.85	5.13	7.74	0.83	4.90	10.67	0.85	4.48	10.09

3.4 Discussion

Developing wearable motion capture systems for unobtrusive daily use is an ongoing challenge. Smart textiles are a promising solution for this problem. In this work, a smart sleeveless shirt was developed by integrating textile-based strain sensors into a commercially available garment. The aim was to investigate the feasibility of this smart garment in capturing

Table 3.5: Performance results of the algorithm in the detection of 3 angles of Ψ (flexion), Θ (rotation), and Φ (lateral bending) for different speeds averaged across all participants

	Ψ			Θ			Φ		
	R^2	RMSE (deg)	NRMSE (%)	R^2	RMSE (deg)	NRMSE (%)	R^2	RMSE (deg)	NRMSE (%)
Slow	0.94	4.12	5.05	0.93	3.35	4.70	0.92	3.26	5.73
Moderate	0.96	3.61	4.55	0.94	3.12	4.09	0.93	3.03	5.10
Fast	0.92	5.06	5.82	0.90	4.12	5.25	0.88	4.02	6.55

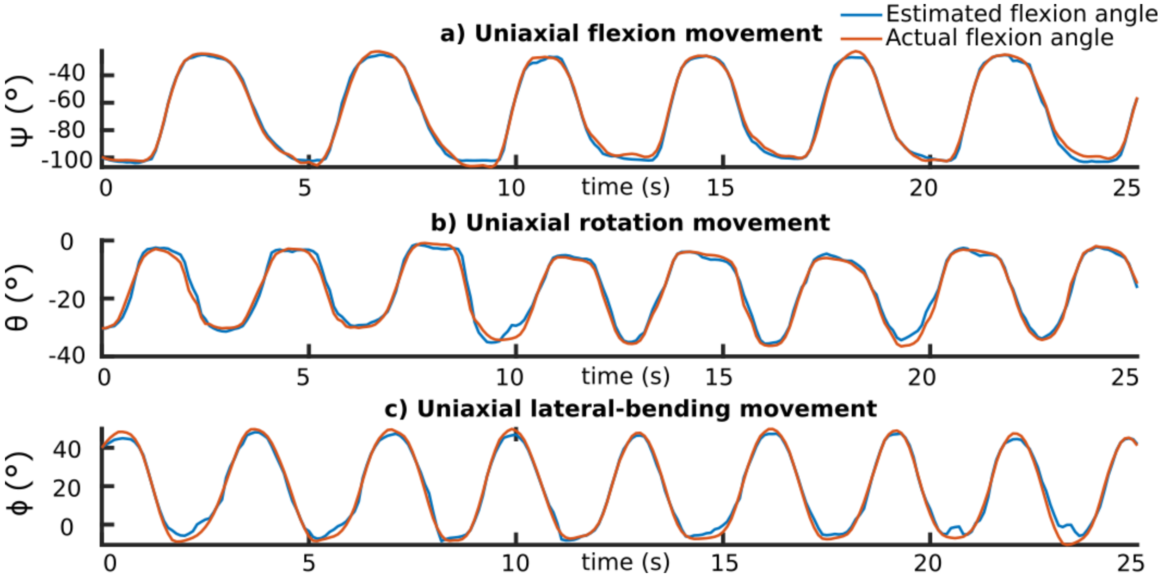

Figure 3.5: Exemplary comparison between the principal reference and estimated Ψ (flexion), Θ (rotation), and Φ (lateral bending) angles in uniaxial movements. (a) Uniaxial flexion movement; (b) Uniaxial rotation movement; (c) Uniaxial lateral bending movement.

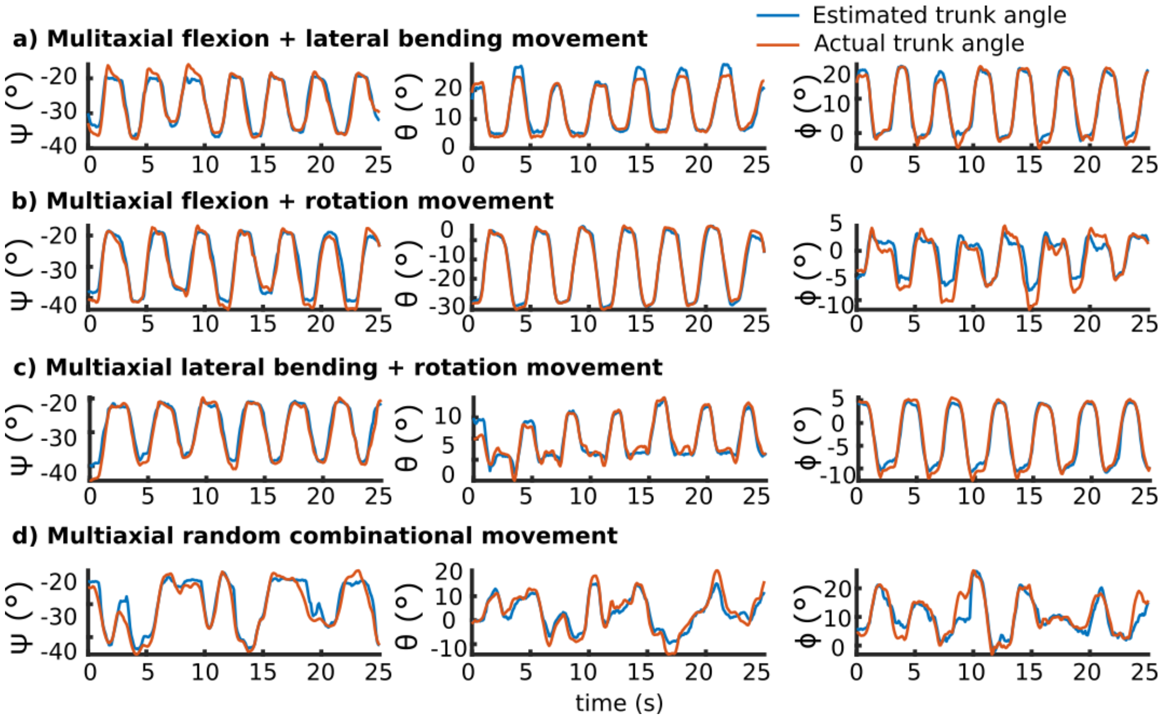

Figure 3.6: Exemplary comparison between 3 kinematic reference and estimated Ψ (flexion), Θ (rotation), and Φ (lateral bending) angles in multiaxial movements. Most estimation errors happened in peaks where the algorithm cannot estimate the exact value. (a) Flexion and lateral bending movement; (b) Flexion and rotation movement; (c) Lateral bending and rotation movement; (d) Multiaxial random combination movement.

all types of planar uniaxial and complicated multiaxial trunk motions to meet objective 1 of this thesis.

The results of this work showed a high agreement between the estimated angles using the smart garment and the angles calculated from the motion capture system. All three angles were estimated with an RMSE of less than 4.26° averaged over all movement conditions. Cuesta et al. suggested that an error between 2° and 5° is likely to be regarded as an acceptable accuracy for wearable systems while extra consideration is required for clinical applications [100]. The accuracy of the proposed system fell in this range and may be sufficient for a wearable motion capture system. Furthermore, there was a high correlation between the estimated angle and real angle with an R^2 higher than 0.91 for all angles. Similar to other systems, this correlation was related to movement complexity [81]. These results showed that in simple planar movements, the estimation followed the real pattern accurately. As the movement became more complex, the level of agreement between the estimated and real angles decreased, but RMSE error was yet below 5° for complex movements, which falls in the acceptable range of accuracy.

The random forest regressor algorithm estimated the trunk flexion, rotation, and lateral bending with RMSE of 4.26°, 3.52°, and 3.40°, respectively. There are several other systems developed for wearable trunk motion tracking. LMM was one of the earliest developed wearable systems and was capable of measuring multiaxial movements of the lumbar part with an error of 1.70° and 0.96°in the frontal and sagittal plane [32]. Considering the complexity of the performed movements in this study, the results of this work is comparable (with slightly higher error) to the LMM system for trunk angular motion measurement. However, LMM is an exoskeleton measuring angles using mechanical connections, which makes the system bulky, obtrusive, and inconvenient for the user to wear daily [101].

IMU-based motion captures are the most common wearable motion captures. Several previous studies have investigated the validity of IMU-based systems for motion analysis [46, 70]. Schall et al. reported accuracy of 4.1° to 6.6° for trunk motion monitoring during a field-based study [101]. Samadani et al. reported errors less than 2° for trunk planar angle measurement [74]. The results of this work compare well to the field-based study, but they fall lower than the Samadani et al. results. It should be emphasized that the data collection protocol in the Samadani et al. report was simple, including only 5 repetitions of planar movements while in other studies with more complicated protocol, an error between 2° to 5° was reported for these IMU-based systems [100]. Considering IMUs limitations of susceptibility to magnetic disturbances and drifting over time[102, 103], the developed smart shirt is comparable to IMU-based systems and superior for environments where magnetic distortions are present. This is the case for most environments in which ferromagnetic materials such as metals are found.

To the best of author's knowledge, there have been limited studies investigating the feasibility of smart garments based on textile-based sensors measuring angles during multiaxial trunk motions. Mokhlespour et al. developed a smart undershirt, capable of measuring planar lumbar movements with 1.3° error when measuring single degree-of-freedom movements [79]. Therefore, no conclusions could be drawn about the application of their system to daily usage where multiaxial movements are inevitable. Mattemann et al. developed a smart catsuit using similar sensors for task classification, although no angle measurement was completed [92]. Yamamoto et al. used stretch sensors fixed to the skin for measuring complicated lumbar motion angles [42]. Complicated movements resulted in errors higher than 10° in measuring trunk flexion-extension angle. This study showed superior results in measuring trunk 3-dimensional angles while performing complicated movements. This shows the feasibility of such smart systems for unobtrusive measurement of kinematic information in multiplanar movements.

Among the 3 estimated kinematic angles, the pitch angle (corresponding to trunk rotation) was estimated with 4.65% error. It has been previously shown that trunk rotation angle was the most challenging to measurement [104]. Using IMU-based systems, this angle was hard to measure because of the susceptibility of IMU sensors to magnetic distortion. As a result, the developed system would be a solution for trunk rotation angle measurement in environments with magnetic susceptibility.

The accuracy of the prototype device did have dependence on the speed of movements, although there was only minimal increase in error during fast movements by only 1.5° for flexion, and 1° for rotation and lateral bending.

This study has some limitations and considerations that should be noted for future studies. First, only one medium size prototype for male participants was developed. However, the participants' body size was variable. Therefore, the prototype did not fit equally between participants (tighter vs. looser fitting). It is suspected that the reason for the weaker performance of the algorithm for some participants could have been the looser fit of the garment. In future studies, prototypes should be produced for each participant, or participants with similar builds should be selected to ensure proper prototype fit. Second, the developed prototype utilized wires for signal transmission. Ideally, wireless data transmission would be implemented into future prototypes. Third, all participants were young healthy individuals. Including a variety of participants with respect to age should be considered. Fourth, the feasibility of the system in an intra-subject approach was investigated. It would be advantageous to develop subject-specific models for smart textile systems because this approach has yielded improved results compared to inter-subject analysis [79]. While this is true, it would be more practical to use such a system for the general population if the system has one global pre-trained model that is trained with data from a sample group of individuals and can be used for all users. This could be attained in future studies by performing specific calibration procedures prior to data collection. For example, Yamamoto et al. suggested measuring sensor data in at least two accurate reference angles for each degree-of-freedom to overcome the inter-subject problem [42]. Fifth, future studies considering more complicated data collection protocols, including tasks such as walking, sitting, and material handling, are required to investigate the feasibility of this system in real applications.

Overall, the developed smart tank top system was able to track multiaxial trunk movements in 3 dimensions with an error less than 4.26°. This shows the great potential of smart textile systems to be used as wearable motion tracking systems. This will provide us with tools for long-term unobtrusive data collection from human movements. This data could supply useful information for applications such as developing personalized interventions to decrease the occurrence of LBP among health care workers.

3.5 Summary

A smart garment prototype employing fiber strain sensors integrated into fabric was developed. The detailed design of this prototype was discussed, and its performance in tracking trunk motions in an exhaustive set of movements was tested in a study with 12 participants. A machine learning random forest regressor was trained and tested in a 3-fold cross-validation approach. Averaging over all participants, this algorithm had 4.26°, 3.52°, and 3.4° error in trunk flexion, rotation, and lateral bending. This chapter addressed the first objective of the thesis in developing a strain-based motion tracking system. Despite the inertial-based motion tracking systems which suffer from drifting over time due to the application of the magnetometers, the developed strain-based prototype solved this problem. However, the complexity of the performed movements caused its accuracy to decrease, demonstrating that further improvement of the strain-based motion tracking system is required for *in situ* applications of the system.

Chapter 4

Towards User-friendly Wearable Platforms for Monitoring Unconstrained Activities

The material of this chapter is excerpted, modified, and reproduced with permission from the following papers that I co-authored:

- A. Rezaei, T.J. Cuthbert, M. Gholami, C. Menon, "Application-Based Production and Testing of a Core-Sheath Fiber Strain Sensor for Wearable Electronics: Feasibility Study of Using the Sensors in Measuring Tri-Axial Trunk Motion Angles", Sensors, vol. 19, no. 19, p. 4288, 2019.
- A. Rezaei, M. Khoshnam, C. Menon, "Towards User-friendly Wearable Platforms for Monitoring Unconstrained Indoor and Outdoor Activities", article in preparation.

Sections of this chapter have been adapted from the above papers to fit the scope and formatting of the thesis.

4.1 Introduction

In this chapter, a novel data fusion algorithm for fusing the strain sensor and gyroscope data is proposed to improve the overall accuracy of motion tracking in 3-dimensional movements. As the accuracy of strain-based motion tracking decreased by the complexity of the movements, the proposed data fusion algorithm should improve the accuracy in the complex 3-dimensional movements. To eliminate the susceptibility to environment magnetic fields, magnetometers were not employed in the proposed algorithm. In this chapter, the kinematic equation describing the relative movement between two dynamic reference frames was discussed, and an unscented Kalman filter was developed for data fusion. The developed smart garment developed in the previous chapter, along with two gyroscope sensors were employed, and the accuracy of the proposed data fusion algorithm was investigated in a study with 10 participants. This chapter addresses the second objective of this thesis for improving the overall accuracy of wearable motion tracking by combining the two prominent types of wearable sensors.

4.2 Proposed Sensor Data Fusion Approach

IMUs are the most common type of wearable sensors and have been used to indirectly calculate the relative orientation between the two sensors' body-fixed coordinate frames $\mathcal{F}1$ and $\mathcal{F}2$. This desired relative orientation is calculated indirectly since each of the sensor units' intermediate orientation with respect to the inertial earth-fixed coordinate frame $\mathcal{G}$ should first be calculated by employing gyroscope, accelerometer, and magnetometer data and then be combined together to produce the relative orientation between $\mathcal{F}1$ and $\mathcal{F}2$. This is mainly because of the accelerometer and magnetometer sensors, which in the measurement update step of the Kalman filter, they can only provide an estimation of the orientation with respect to the frame $\mathcal{G}$. Kalman filter has therefore been applied to each IMU unit sensors' data separately to estimate the IMU's intermediate orientation relative to the earth-fixed inertial frame. However, other types of wearable sensors, such as strain sensors, are capable of directly estimating the relative orientation.

In this work, it is proposed that if an estimation of the relative orientation between the two IMUs is by some means available, this estimation could be combined with the angular velocities of the two IMUs in one Kalman filter structure to improve the estimated orientation and eliminate the need for accelerometers, magnetometers, and their associated limitations. In the context of wearable sensors, textile integrated fiber strain sensors can provide this estimation by employing machine learning approaches and have been used in this work to test the proposed solution. The overall structure of this solution is shown in

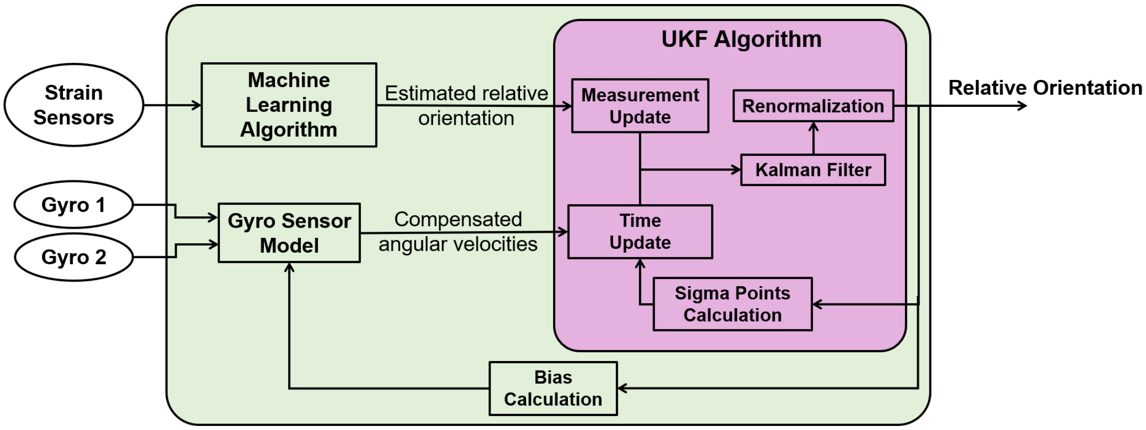

Figure 4.1: The gyroscope-strain sensor data fusion structure using machine learning and UKF

Figure 4.1. An unscented Kalman filter was implemented to directly estimate the relative orientation between the two dynamic coordinate reference frames $\mathcal{F}1$ and $\mathcal{F}2$, both with nonzero angular velocity, eliminating the intermediate orientation calculation step. In this approach, both sensors' angular velocity vectors were coupled together as the input to the time update step of the filter while the measurement update was provided to the filter using the strain sensor information. A machine learning algorithm was applied to the strain sensor signals to predict the relative orientation between the two sensor units. This prediction was then used as the measurement update of the filter. Using this approach would consequently substitute the two IMU units(six sensors) used in the conventional filtering approaches with an array of fiber strain sensors integrated into the regular clothing and two gyroscope sensors. Although the application of this algorithm for trunk motion tracking has been represented in this chapter, this algorithm is a general solution and can be applied for measuring all human joints kinematic information by fusing the data from two gyroscope sensors and other types of wearable sensors, as long as they are capable of providing an estimation of the relative desired orientation.

4.3 Unscented Kalman Filter

4.3.1 Notation

Euler angles, rotation matrix, and unit quaternions are among the common representations of the orientation of a reference frame. In this work, unit quaternions were used for representing the orientation and rotation of a reference frame, since they are a relatively computationally efficient method and do not suffer from singularity problems in contrast to the other two methods [105]. Considering the two frames $\mathcal{F}1$ and $\mathcal{F}2$, ${}^{\mathcal{F}2}_{\mathcal{F}1}\bar{q}$ shows the relative orientation of $\mathcal{F}2$ with respect to $\mathcal{F}1$. This is a unit quaternion with a norm of 1 and consists of a scalar part q_4 and a vector part $\mathbf{q} = [q_1, q_2, q_3]^T$ and is defined as

$$
{}^{\mathcal{F}2}_{\mathcal{F}1}\bar{q} = \begin{bmatrix} \mathbf{q} \\ q_4 \end{bmatrix} = [q_1 \; q_2 \; q_3 \; q_4]^T \tag{4.1}
$$

This quaternion has the equivalent rotation matrix ${}^{\mathcal{F}2}_{\mathcal{F}1}\boldsymbol{C}$. If ${}^{\mathcal{F}1}\mathbf{u}$ denotes the vector $\mathbf{u}$ in frame $\mathcal{F}1$, then

$$
\begin{bmatrix} {}^{\mathcal{F}2}\mathbf{u} \\ 0 \end{bmatrix} = {}^{\mathcal{F}2}_{\mathcal{F}1}\bar{q} \otimes \begin{bmatrix} {}^{\mathcal{F}1}\mathbf{u} \\ 0 \end{bmatrix} \otimes {}^{\mathcal{F}2}_{\mathcal{F}1}\bar{q}^{*} \tag{4.2}
$$

transforms the vector $\mathbf{u}$ to frame $\mathcal{F}2$ denoted as ${}^{\mathcal{F}2}\mathbf{u}$. In this formula, ${}^{\mathcal{F}2}_{\mathcal{F}1}\bar{q}^{*}$ is the conjugate of ${}^{\mathcal{F}2}_{\mathcal{F}1}\bar{q}$ defined as

$$
{}^{\mathcal{F}2}_{\mathcal{F}1}\bar{q}^{*} = \begin{bmatrix} -\mathbf{q} \\ q_4 \end{bmatrix} \tag{4.3}
$$

and symbol $\otimes$ represents the quaternion multiplication, Similarly, vector ${}^{\mathcal{F}1}\mathbf{u}$ can be transformed to $\mathcal{F}2$ using the rotaion matrix with the equation ${}^{\mathcal{F}2}\mathbf{u} = {}^{\mathcal{F}2}_{\mathcal{F}1}\boldsymbol{C}\, {}^{\mathcal{F}1}\mathbf{u}$. The relationship between this rotation matrix and the corresponding unit quaternion ${}^{\mathcal{F}2}_{\mathcal{F}1}\bar{q}$ is as follows

$$
{}^{\mathcal{F}2}_{\mathcal{F}1}\boldsymbol{C} \;=\; (2q_4^2 - 1)\boldsymbol{I}_{3\times 3} \;-\; 2q_4\lfloor \boldsymbol{q}\times \rfloor \;+\; 2\boldsymbol{q}\boldsymbol{q}^T \tag{4.4}
$$

in which $\lfloor \boldsymbol{q}\times \rfloor$ is a skew-symmetric function defined as

$$\lfloor \boldsymbol{q}\times \rfloor = \begin{bmatrix} 0 & -q_3 & q_2 \\ q_3 & 0 & -q_1 \\ -q_2 & q_1 & 0 \end{bmatrix} \tag{4.5}$$

4.3.2 Relative Orientation Kinematic Equation

The kinematic equation of the relative orientation between the two reference frames is required for the UKF. Suppose that ${}^{\mathcal{F}2}\boldsymbol{\omega}_{\mathcal{F}2}$ is the angular velocity of the reference frame $\mathcal{F}2$ expressed in the same frame. Then the time derivative of the orientation of $\mathcal{F}2$ with respect to the inertial frame $\mathcal{G}$ with zero angular velocity is

$${}^{\mathcal{F}2}_{\mathcal{G}}\dot{\bar{q}} = \frac{1}{2}\boldsymbol{\Xi}({}^{\mathcal{F}2}_{\mathcal{G}}\bar{q})\,{}^{\mathcal{F}2}\boldsymbol{\omega}_{\mathcal{F}2} \tag{4.6}$$

where matrix $\boldsymbol{\Xi}(\bar{q})$ is defined as

$$\boldsymbol{\Xi}(\bar{q}) = \begin{bmatrix} \lfloor \boldsymbol{q}\times \rfloor + q_4 \boldsymbol{I}_{3\times 3} \\ -\boldsymbol{q}^T \end{bmatrix} = \begin{bmatrix} q_4 & -q_3 & q_2 \\ q_3 & q_4 & -q_1 \\ -q_2 & q_1 & q_4 \\ -q_1 & -q_2 & -q_3 \end{bmatrix} \tag{4.7}$$

If the orientation of $\mathcal{F}2$ was expressed with respect to the frame $\mathcal{F}1$ which has the angular velocity of ${}^{\mathcal{F}1}\boldsymbol{\omega}_{\mathcal{F}1}$, equation 4.6 should change to the following format

$${}^{\mathcal{F}2}_{\mathcal{F}1}\dot{\bar{q}} = \frac{1}{2}\boldsymbol{\Xi}({}^{\mathcal{F}2}_{\mathcal{F}1}\bar{q})\,{}^{\mathcal{F}2}\boldsymbol{\omega}_{\mathcal{F}2\mathcal{F}1} \tag{4.8}$$

in which ${}^{\mathcal{F}2}\boldsymbol{\omega}_{\mathcal{F}2\mathcal{F}1}$ is the relative angular velocity between the two frames expressed in the frame $\mathcal{F}2$. This equation and the rest of this section is adopted from [106]. Suppose the variable $\Delta\omega$ is defined as

$$\Delta\boldsymbol{\omega} = {}^{\mathcal{F}2}\boldsymbol{\omega}_{\mathcal{F}2} - {}^{\mathcal{F}1}\boldsymbol{\omega}_{\mathcal{F}1} = [\Delta\boldsymbol{\omega}_x \; \Delta\boldsymbol{\omega}_y \; \Delta\boldsymbol{\omega}_z]^T \tag{4.9}$$

and shows the difference between the two angular velocity vectors. The relative angular velocity can then be stated as

$$ {}^{\mathcal{F}2}\boldsymbol{\omega}_{\mathcal{F}2\mathcal{F}1} = {}^{\mathcal{F}2}\boldsymbol{\omega}_{\mathcal{F}2} - {}^{\mathcal{F}2}_{\mathcal{F}1}\boldsymbol{C}\,{}^{\mathcal{F}1}\boldsymbol{\omega}_{\mathcal{F}1} = \Delta\boldsymbol{\omega} + (\boldsymbol{I}_{3\times3} - {}^{\mathcal{F}2}_{\mathcal{F}1}\boldsymbol{C})^{\mathcal{F}1}\boldsymbol{\omega}_{\mathcal{F}1} \tag{4.10} $$

Substituting equation 4.10 in 4.8, the time derivative of the relative unit quaternion is

$$ {}^{\mathcal{F}2}_{\mathcal{F}1}\dot{\bar{q}} = \frac{1}{2}\boldsymbol{\Xi}({}^{\mathcal{F}2}_{\mathcal{F}1}\bar{q})\,\Delta\boldsymbol{\omega} + \frac{1}{2}\boldsymbol{\Xi}({}^{\mathcal{F}2}_{\mathcal{F}1}\bar{q})\,(\boldsymbol{I}_{3\times3} - {}^{\mathcal{F}2}_{\mathcal{F}1}\boldsymbol{C})^{\mathcal{F}1}\boldsymbol{\omega}_{\mathcal{F}1} \tag{4.11} $$

As it is shown in [106], the following relationships can be considered for any vector

$$ \lfloor\boldsymbol{q}\times\rfloor\lfloor\boldsymbol{q}\times\rfloor + \boldsymbol{q}^T\boldsymbol{q}\boldsymbol{I} - \boldsymbol{q}\boldsymbol{q}^T = 0_{3\times3},\ \ \boldsymbol{q}^T\boldsymbol{q}\boldsymbol{q}\boldsymbol{q}^T = \boldsymbol{q}\boldsymbol{q}^T\boldsymbol{q}\boldsymbol{q}^T \tag{4.12a} $$

$$ \boldsymbol{q}\boldsymbol{q}^T\lfloor\boldsymbol{q}\times\rfloor = 0_{3\times3},\ \ \lfloor\boldsymbol{q}\times\rfloor\boldsymbol{q}\boldsymbol{q}^T = 0_{3\times3} \tag{4.12b} $$

Using these relationships, the term $\frac{1}{2}\boldsymbol{\Xi}({}^{\mathcal{F}2}_{\mathcal{F}1}\bar{q})\,(\boldsymbol{I}_{3\times3} - {}^{\mathcal{F}2}_{\mathcal{F}1}\boldsymbol{C})$ in equation 4.11 can therefore be simplified to

$$ \frac{1}{2}\boldsymbol{\Xi}({}^{\mathcal{F}2}_{\mathcal{F}1}\bar{q})\,(\boldsymbol{I}_{3\times3} - {}^{\mathcal{F}2}_{\mathcal{F}1}\boldsymbol{C}) = \begin{bmatrix} \lfloor\boldsymbol{q}\times\rfloor \\ 0_{1\times3} \end{bmatrix} \tag{4.13} $$

and therefore equation 4.11 can be simplified to

$$ {}^{\mathcal{F}2}_{\mathcal{F}1}\dot{\bar{q}} = \frac{1}{2}\boldsymbol{\Xi}({}^{\mathcal{F}2}_{\mathcal{F}1}\bar{q})\,\Delta\boldsymbol{\omega} + \begin{bmatrix} \lfloor\boldsymbol{q}\times\rfloor \\ 0_{1\times3} \end{bmatrix} {}^{\mathcal{F}1}\boldsymbol{\omega}_{\mathcal{F}1} \tag{4.14} $$

Furthermore, equation 4.14 can be expressed in the following format

$$ {}^{\mathcal{F}2}_{\mathcal{F}1}\dot{\bar{q}} = (\frac{1}{2}\boldsymbol{\Omega}(\Delta\boldsymbol{\omega}) - \begin{bmatrix} \lfloor{}^{\mathcal{F}1}\boldsymbol{\omega}_{\mathcal{F}1}\times\rfloor & 0_{3\times1} \\ 0_{1\times3} & 0 \end{bmatrix})\,{}^{\mathcal{F}2}_{\mathcal{F}1}\bar{q} = \boldsymbol{F}({}^{\mathcal{F}2}\boldsymbol{\omega}_{\mathcal{F}2}\,,\,{}^{\mathcal{F}1}\boldsymbol{\omega}_{\mathcal{F}1})\,{}^{\mathcal{F}2}_{\mathcal{F}1}\bar{q} \tag{4.15} $$

in which the matrix $\boldsymbol{\Omega}(\Delta\boldsymbol{\omega})$ is defined as

$$\boldsymbol{\Omega}(\Delta\boldsymbol{\omega}) = \begin{bmatrix} 0 & \Delta\boldsymbol{\omega}_z & -\Delta\boldsymbol{\omega}_y & \Delta\boldsymbol{\omega}_x \\ -\Delta\boldsymbol{\omega}_z & 0 & \Delta\boldsymbol{\omega}_x & \Delta\boldsymbol{\omega}_y \\ \Delta\boldsymbol{\omega}_y & -\Delta\boldsymbol{\omega}_x & 0 & \Delta\boldsymbol{\omega}_z \\ -\Delta\boldsymbol{\omega}_x & -\Delta\boldsymbol{\omega}_y & -\Delta\boldsymbol{\omega}_z & 0 \end{bmatrix} \tag{4.16}$$

The formula ${}^{\mathcal{F}2}_{\mathcal{F}1}\dot{\overline{q}} = \boldsymbol{F}\, {}^{\mathcal{F}2}_{\mathcal{F}1}\overline{q}$ is a differential equation and describes the time derivative of the orientation between two dynamic reference frames. Solving this equation in the discrete format would allow calculating ${}^{\mathcal{F}2}_{\mathcal{F}1}\overline{q}(t_k)$ having ${}^{\mathcal{F}2}_{\mathcal{F}1}\overline{q}(t_{k-1})$ and the angular velocity vectors of the two frames at t_{k-1}. The solution to this equation can generally be formulated as [107, p. 40]

$${}^{\mathcal{F}2}_{\mathcal{F}1}\overline{q}(t_k) = \boldsymbol{\Theta}(t_k, t_{k-1})\, {}^{\mathcal{F}2}_{\mathcal{F}1}\overline{q}(t_{k-1}) \tag{4.17}$$

Under the certain assumption that both angular velocities ${}^{\mathcal{F}2}\boldsymbol{\omega}_{\mathcal{F}2}$ and ${}^{\mathcal{F}1}\boldsymbol{\omega}_{\mathcal{F}1}$ were constant during the time interval $\Delta t = t_k - t_{k-1}$ between t_{k-1} and t_k, the matrix $\boldsymbol{F}({}^{\mathcal{F}2}\boldsymbol{\omega}_{\mathcal{F}2}\,, {}^{\mathcal{F}1}\boldsymbol{\omega}_{\mathcal{F}1})$ would be constant and the term $\boldsymbol{\Theta}(t_k, t_{k-1})$ in equation 4.17 can be expressed in the form of a matrix exponential as

$$\boldsymbol{\Theta}(t_k, t_{k-1}) = \boldsymbol{\Theta}(\Delta t) = exp(\boldsymbol{F}\Delta t) = \boldsymbol{I}_{4\times4} + \boldsymbol{F}\Delta t + \frac{1}{2!}\boldsymbol{F}^2\Delta t^2 + \frac{1}{3!}\boldsymbol{F}^3\Delta t^3 + \cdots \tag{4.18}$$

Assuming the value of Δt is small, second and higher-order terms of Δt are negligible, and equation 4.17 can therefore be expressed as

$${}^{\mathcal{F}2}_{\mathcal{F}1}\overline{q}(t_k) = (\boldsymbol{I}_{4\times4} + \boldsymbol{F}({}^{\mathcal{F}2}\boldsymbol{\omega}_{\mathcal{F}2}\,, {}^{\mathcal{F}1}\boldsymbol{\omega}_{\mathcal{F}1})\,\Delta t)\, {}^{\mathcal{F}2}_{\mathcal{F}1}\overline{q}(t_{k-1}) \tag{4.19}$$

4.3.3 Gyro Sensor Modeling

Adopted from [108], the measured angular velocity $\boldsymbol{\omega}_m$ by gyro sensor in its local frame can be written as follows

$$\boldsymbol{\omega}_m = \boldsymbol{\omega}_{body} + \boldsymbol{b} + {}^{v}\boldsymbol{\eta} \tag{4.20a}$$

$$\dot{\boldsymbol{b}} = {}^{u}\boldsymbol{\eta} \tag{4.20b}$$

where $\boldsymbol{\omega}_{body}$ is the real angular velocity of the frame, $\boldsymbol{b}$ is a random-walk process and shows sensor bias vector, and ${}^{v}\boldsymbol{\eta}$ and ${}^{u}\boldsymbol{\eta}$ are independent white Gaussian processes with zero mean and covariance matrices ${}^{v}\sigma^2\boldsymbol{I}_{3\times3}$ and ${}^{u}\sigma^2\boldsymbol{I}_{3\times3}$ respectively. ${}^{v}\boldsymbol{\eta}$ shows gyro measurement noise and ${}^{u}\boldsymbol{\eta}$ depicts gyro bias change noise. Based on equation 4.20a, the bias compensated angular velocity $\hat{\boldsymbol{\omega}}$ is $\hat{\boldsymbol{\omega}} = \boldsymbol{\omega}_m - \boldsymbol{b} = \boldsymbol{\omega}_{body} + {}^{v}\boldsymbol{\eta}$. Integrating equation 4.20b propagates the bias vector over time as follows

$$\boldsymbol{b}(t_k) = \boldsymbol{b}(t_{k-1}) + {}^{u}\boldsymbol{\eta}(t_{k-1}) \tag{4.21}$$

4.3.4 System Model

Process Model

The state vector $\boldsymbol{x}$ comprised the relative quaternion ${}^{\mathcal{F}2}_{\mathcal{F}1}\bar{q}$, frame $\mathcal{F}2$ gyro bias vector $\boldsymbol{b}_{\mathcal{F}2}$, and frame $\mathcal{F}1$ gyro bias vector $\boldsymbol{b}_{\mathcal{F}1}$

$$\boldsymbol{x} = \begin{bmatrix} {}^{\mathcal{F}2}_{\mathcal{F}1}\bar{q} \\ \boldsymbol{b}_{\mathcal{F}2} \\ \boldsymbol{b}_{\mathcal{F}1} \end{bmatrix} \tag{4.22}$$

Using equations 4.19 and 4.21, the process model was

$$\begin{bmatrix} {}^{\mathcal{F}2}_{\mathcal{F}1}\bar{q}(t_k) \\ \boldsymbol{b}_{\mathcal{F}2}(t_k) \\ \boldsymbol{b}_{\mathcal{F}1}(t_k) \end{bmatrix} = \boldsymbol{A} \begin{bmatrix} {}^{\mathcal{F}2}_{\mathcal{F}1}\bar{q}(t_{k-1}) \\ \boldsymbol{b}_{\mathcal{F}2}(t_{k-1}) \\ \boldsymbol{b}_{\mathcal{F}1}(t_{k-1}) \end{bmatrix} + \mathbf{w}(t_{k-1}) \tag{4.23}$$

in which matrix $\boldsymbol{A}$ is

$$\boldsymbol{A} = \begin{bmatrix} \boldsymbol{I}_{4\times 4} + \boldsymbol{F}\,\Delta t & 0_{4\times 3} & 0_{4\times 3} \\ 0_{3\times 4} & \boldsymbol{I}_{3\times 3} & 0_{3\times 3} \\ 0_{3\times 4} & 0_{3\times 3} & \boldsymbol{I}_{3\times 3} \end{bmatrix} \tag{4.24}$$

and was calculated using the bias compensated angular velocities ${}^{\mathcal{F}2}\hat{\boldsymbol{\omega}}_{\mathcal{F}2}(t_{k-1})$ and ${}^{\mathcal{F}1}\hat{\boldsymbol{\omega}}_{\mathcal{F}1}(t_{k-1})$. The vector $\mathbf{w}(t_{k-1})$ is the process noise vector

$$\mathbf{w}(t_{k-1}) = \begin{bmatrix} {}^{v}\boldsymbol{w}(t_{k-1}) \\ {}^{u}\boldsymbol{\eta}_{\mathcal{F}2}(t_{k-1}) \\ {}^{u}\boldsymbol{\eta}_{\mathcal{F}1}(t_{k-1}) \end{bmatrix} \tag{4.25}$$

where ${}^{v}\boldsymbol{w}(t_{k-1})$ demonstrates how both gyros' measurement noise vectors ${}^{v}\boldsymbol{\eta}_{\mathcal{F}2}$ and ${}^{v}\boldsymbol{\eta}_{\mathcal{F}1}$ generate process noise vector by undergoing through the process model (equation 4.14). This vector is equal to

$${}^{v}\boldsymbol{w}(t_{k-1}) = -\frac{\Delta t}{2}[\boldsymbol{\Xi}({}^{\mathcal{F}2}_{\mathcal{F}1}\bar{q}(t_{k-1}))\,({}^{v}\boldsymbol{\eta}_{\mathcal{F}2}(t_{k-1}) -{}^{v}\boldsymbol{\eta}_{\mathcal{F}1}(t_{k-1})) + 2\begin{bmatrix} \lfloor \boldsymbol{q}(t_{k-1})\times \rfloor \\ 0_{1\times 3} \end{bmatrix} {}^{v}\boldsymbol{\eta}_{\mathcal{F}1}(t_{k-1})] \tag{4.26}$$

Assuming the two vectors ${}^{v}\boldsymbol{\eta}_{\mathcal{F}1} = [{}^{v}\eta_{\mathcal{F}1x}, {}^{v}\eta_{\mathcal{F}1y}, {}^{v}\eta_{\mathcal{F}1z}]^T$ and ${}^{v}\boldsymbol{\eta}_{\mathcal{F}2} = [{}^{v}\eta_{\mathcal{F}2x}, {}^{v}\eta_{\mathcal{F}2y}, {}^{v}\eta_{\mathcal{F}2z}]^T$, equation 4.26 can therefore be expressed as

$${}^{v}\boldsymbol{w} = -\frac{\Delta t}{2}\begin{bmatrix} q_4({}^{v}\eta_{\mathcal{F}2x} -{}^{v}\eta_{\mathcal{F}1x}) - q_3({}^{v}\eta_{\mathcal{F}2y} +{}^{v}\eta_{\mathcal{F}1y}) + q_2({}^{v}\eta_{\mathcal{F}2z} +{}^{v}\eta_{\mathcal{F}1z}) \\ q_3({}^{v}\eta_{\mathcal{F}2x} +{}^{v}\eta_{\mathcal{F}1x}) + q_4({}^{v}\eta_{\mathcal{F}2y} -{}^{v}\eta_{\mathcal{F}1y}) - q_1({}^{v}\eta_{\mathcal{F}2z} +{}^{v}\eta_{\mathcal{F}1z}) \\ -q_2({}^{v}\eta_{\mathcal{F}2x} +{}^{v}\eta_{\mathcal{F}1x}) + q_1({}^{v}\eta_{\mathcal{F}2y} +{}^{v}\eta_{\mathcal{F}1y}) + q_4({}^{v}\eta_{\mathcal{F}2z} -{}^{v}\eta_{\mathcal{F}1z}) \\ -q_1({}^{v}\eta_{\mathcal{F}2x} -{}^{v}\eta_{\mathcal{F}1x}) - q_2({}^{v}\eta_{\mathcal{F}2y} -{}^{v}\eta_{\mathcal{F}1y}) - q_3({}^{v}\eta_{\mathcal{F}2z} -{}^{v}\eta_{\mathcal{F}1z}) \end{bmatrix} \tag{4.27}$$

${}^{v}\boldsymbol{w}(t_{k-1})$, ${}^{u}\boldsymbol{\eta}_{\mathcal{F}2}(t_{k-1})$, and ${}^{u}\boldsymbol{\eta}_{\mathcal{F}1}(t_{k-1})$ are independent processes and the covariance of the process noise $\mathbf{w}(t_{k-1})$ is therefore defined as

$$\boldsymbol{Q} = E[\mathbf{w}\mathbf{w}^T] = \begin{bmatrix} {}^{v}\boldsymbol{Q} & 0_{4\times 3} & 0_{4\times 3} \\ 0_{3\times 4} & {}^{u}\sigma^2_{\mathcal{F}2}\boldsymbol{I}_{3\times 3} & 0_{3\times 3} \\ 0_{3\times 4} & 0_{3\times 3} & {}^{u}\sigma^2_{\mathcal{F}1}\boldsymbol{I}_{3\times 3} \end{bmatrix} \tag{4.28}$$

where the term ${}^{v}\boldsymbol{Q}$ is the coavariance matrix of ${}^{v}\boldsymbol{w}(t_{k-1})$ and is equal to ${}^{v}\boldsymbol{Q} = E[{}^{v}\boldsymbol{w}{}^{v}\boldsymbol{w}^T]$. As defined before, it is known that $E[{}^{v}\boldsymbol{\eta}_{\mathcal{F}1}\,{}^{v}\boldsymbol{\eta}_{\mathcal{F}1}^T] = {}^{v}\sigma_{\mathcal{F}1}^2\boldsymbol{I}_{3\times3}$ and $E[{}^{v}\boldsymbol{\eta}_{\mathcal{F}2}\,{}^{v}\boldsymbol{\eta}_{\mathcal{F}2}^T] = {}^{v}\sigma_{\mathcal{F}2}^2\boldsymbol{I}_{3\times3}$. The vector ${}^{v}\boldsymbol{w}(t_{k-1})$ is also defined in the equation 4.27 and therefore its covariance can be defined as

$$ {}^{v}\boldsymbol{Q} = E[{}^{v}\boldsymbol{w}{}^{v}\boldsymbol{w}^T] = \begin{bmatrix} Q_{11} & Q_{12} & Q_{13} & Q_{14} \\ Q_{21} & Q_{22} & Q_{23} & Q_{24} \\ Q_{31} & Q_{32} & Q_{33} & Q_{34} \\ Q_{41} & Q_{42} & Q_{43} & Q_{44} \end{bmatrix} \tag{4.29} $$

which the terms in this matrix are calculated as follows

$$ Q_{11} = \frac{\Delta t^2}{4}(q_4^2 + q_3^2 + q_2^2)({}^{u}\sigma_{\mathcal{F}2}^2 +{}^{u} \sigma_{\mathcal{F}1}^2) \tag{4.30a} $$

$$ Q_{22} = \frac{\Delta t^2}{4}(q_3^2 + q_4^2 + q_1^2)({}^{u}\sigma_{\mathcal{F}2}^2 +{}^{u} \sigma_{\mathcal{F}1}^2) \tag{4.30b} $$

$$ Q_{33} = \frac{\Delta t^2}{4}(q_2^2 + q_1^2 + q_4^2)({}^{u}\sigma_{\mathcal{F}2}^2 +{}^{u} \sigma_{\mathcal{F}1}^2) \tag{4.30c} $$

$$ Q_{44} = \frac{\Delta t^2}{4}(q_1^2 + q_2^2 + q_3^2)({}^{u}\sigma_{\mathcal{F}2}^2 +{}^{u} \sigma_{\mathcal{F}1}^2) \tag{4.30d} $$

$$ Q_{12} = Q_{21} = \frac{\Delta t^2}{4}(-q_1q_2({}^{u}\sigma_{\mathcal{F}2}^2 +{}^{u} \sigma_{\mathcal{F}1}^2)) \tag{4.30e} $$

$$ Q_{13} = Q_{31} = \frac{\Delta t^2}{4}(-q_1q_3({}^{u}\sigma_{\mathcal{F}2}^2 +{}^{u} \sigma_{\mathcal{F}1}^2)) \tag{4.30f} $$

$$ Q_{14} = Q_{41} = \frac{\Delta t^2}{4}(-q_1q_4({}^{u}\sigma_{\mathcal{F}2}^2 +{}^{u} \sigma_{\mathcal{F}1}^2)) \tag{4.30g} $$

$$ Q_{23} = Q_{32} = \frac{\Delta t^2}{4}(-q_2q_3({}^{u}\sigma_{\mathcal{F}2}^2 +{}^{u} \sigma_{\mathcal{F}1}^2)) \tag{4.30h} $$

$$ Q_{24} = Q_{42} = \frac{\Delta t^2}{4}(-q_2q_4({}^{u}\sigma_{\mathcal{F}2}^2 +{}^{u} \sigma_{\mathcal{F}1}^2)) \tag{4.30i} $$

$$ Q_{34} = Q_{43} = \frac{\Delta t^2}{4}(-q_3q_4({}^{u}\sigma_{\mathcal{F}2}^2 +{}^{u} \sigma_{\mathcal{F}1}^2)) \tag{4.30j} $$

These terms can be simplified and be shown as

$$ {}^{v}\boldsymbol{Q} = \frac{\Delta t^2}{4} \begin{bmatrix} 1-q_1^2 & -q_1q_2 & -q_1q_3 & -q_1q_4 \\ -q_2q_1 & 1-q_2^2 & -q_2q_3 & -q_2q_4 \\ -q_3q_1 & -q_3q_2 & 1-q_3^2 & -q_3q_4 \\ -q_4q_1 & -q_4q_2 & -q_4q_3 & 1-q_4^2 \end{bmatrix} ({}^{u}\sigma_{\mathcal{F}2}^2 +{}^{u} \sigma_{\mathcal{F}1}^2) \tag{4.31} $$

Measurement Model

Measurement model relates the state vector $\boldsymbol{x}$ to the measurement vector $\boldsymbol{y}$. The vector $\boldsymbol{y}$ includes the Euler angles representation of the relative orientation between the two frames $\mathcal{F}2$ and $\mathcal{F}1$ depicted as $\boldsymbol{y} = [\psi, \theta, \phi]^T$ in which ψ, θ, and ϕ are roll, pitch and yaw angles respectively. The measurement model has the general form of

$$\boldsymbol{y}(t_k) = \boldsymbol{H}(\boldsymbol{x}(t_k)) + \mathbf{v}(t_k) \tag{4.32}$$

in which H is a nonlinear function and vector $\mathbf{v}(t_k)$ shows the measurement noise. Considering the ZYX convention for Euler angles, the function H is defined as follows

$$\boldsymbol{H}(\boldsymbol{x}(t_k)) = \begin{bmatrix} \arctan(\dfrac{2q_2q_3 + 2q_1q_4}{1 - 2q_1^2 - 2q_2^2}) \\ \arcsin(2q_1q_3 - 2q_2q_4) \\ \arctan(\dfrac{2q_1q_2 + 2q_3q_4}{1 - 2q_2^2 - 2q_3^2}) \end{bmatrix} \tag{4.33}$$

Vector $\mathrm{v}(t_k)$ is a white zero-mean Gaussian process which its covariance matrix is shown as follows

$$\boldsymbol{R} = E[\boldsymbol{v}\boldsymbol{v}^T] \; = \; {}^{m}\sigma^2 \boldsymbol{I}_{3\times 3} \tag{4.34}$$

In this work, an estimation of the measurement vector $\boldsymbol{y} = [\psi, \theta, \phi]^T$ was available from the strain sensor and the matrix $\boldsymbol{R}$ value was set as a tuning parameter of the filter.

4.3.5 Unscented Kalman Filter

The UKF has two different forms in terms of how the states vector is formed. It can be in the additive form or the augmented form [109]. Augmented form comprises adding the process and the measurement noise vectors to the state vector and augmenting its dimension, while in the additive form, these noises are only added in the system's model equations. In this work, the additive form of the UKF was adopted [110]. In the following, the steps of the UKF are described.

Initialization

State vector $\boldsymbol{x}$ is a random variable with mean value $\hat{\boldsymbol{x}} = E[\boldsymbol{x}]$, the covariance matrix $\hat{\boldsymbol{P}}_{\boldsymbol{x}} = E[(\boldsymbol{x}-\hat{\boldsymbol{x}})(\boldsymbol{x}-\hat{\boldsymbol{x}})^T]$, and the length L. The initial value of these statistics are required to start the recursive process of the UKF and were assumed to be known at time t_0.

Sigma Vectors and Time Update

The UKF is based on generating sigma vectors to approximate the statistics of the output of a nonlinear function having the statistics of its random input variables [62]. Sigma vectors are a minimal set of carefully selected weighted vectors. Employing these points, the linearization process which is an essential part of the EKF is eliminated. Herein, sigma points were generated for the state vector $\boldsymbol{x}$ which undergoes through equations 4.23 and 4.32. Assuming $\hat{\boldsymbol{x}}(t_{k-1})$, $\hat{\boldsymbol{P}}_{\boldsymbol{x}}(t_{k-1})$, and $\boldsymbol{Q}(t_{k-1})$ were known at time t_{k-1}, $2L+1$ sigma vectors were thus defined as the columns of a matrix $\boldsymbol{\mathcal{X}}(t_{k-1})$ with the corresponding weights W^c and W^m [62, 110]. The column $\mathcal{X}_i$ with weights W_i^c and W_i^m was calculated using

$$\mathcal{X}_0 = \hat{\boldsymbol{x}}(t_{k-1}) \tag{4.35a}$$

$$\mathcal{X}_i = \hat{\boldsymbol{x}}(t_{k-1}) + \left(\sqrt{(L+\lambda)(\hat{\boldsymbol{P}}_{\boldsymbol{x}}(t_{k-1}) + \boldsymbol{Q}(t_{k-1}))}\right)_i \qquad i = 1, \cdots, L \tag{4.35b}$$

$$\mathcal{X}_i = \hat{\boldsymbol{x}}(t_{k-1}) - \left(\sqrt{(L+\lambda)(\hat{\boldsymbol{P}}_{\boldsymbol{x}}(t_{k-1}) + \boldsymbol{Q}(t_{k-1}))}\right)_{i-L} \qquad i = L+1, \cdots, 2L \tag{4.35c}$$

$$W_0^m = \frac{\lambda}{L+\lambda} \tag{4.35d}$$

$$W_0^c = \frac{\lambda}{L+\lambda} + 1 - \alpha^2 + \beta \tag{4.35e}$$

$$W_i^m = W_i^c = \frac{\lambda}{2(L+\lambda)} \quad i = 1, \cdots, 2L \tag{4.35f}$$

where α is a scaling parameter ranging from a small number (10^{-3}) to 1, $\lambda = \alpha^2(L+\kappa) - L$ in which κ is a secondary scaling parameter usually with 0 value, and β, with optimal value 2 for Gaussian variables includes the prior knowledge of $\hat{\boldsymbol{x}}$ into the process. In this work, α, κ, and β were set to 10^{-3}, 0, and 2 respectively. $(\sqrt{(L+\lambda)(\hat{\boldsymbol{P}}_{\boldsymbol{x}}(t_{k-1}) + \boldsymbol{Q}(t_{k-1}))})_i$ is the ith row of the matrix square root. The sigma vectors were then undergone the equation 4.23 to generate *a priori* state estimate $\hat{\boldsymbol{x}}^-(t_k)$ and covariance matrix $\hat{\boldsymbol{P}}_{\boldsymbol{x}}^-(t_k)$ estimate at time t_k.

The steps are shown below

$$\mathcal{X}_i(t_k|t_{k-1}) = \boldsymbol{A}\mathcal{X}_i(t_{k-1}) \quad i = 0, \cdots, 2L \tag{4.36a}$$

$$\hat{\boldsymbol{x}}^-(t_k) = \sum_{i=0}^{2L} W_i^m \mathcal{X}_i(t_k|t_{k-1}) \tag{4.36b}$$

$$\hat{\boldsymbol{P}}_{\boldsymbol{x}}^-(t_k) = \sum_{i=0}^{2L} W_i^c [\mathcal{X}_i(t_k|t_{k-1}) - \hat{\boldsymbol{x}}^-(t_k)][\mathcal{X}_i(t_k|t_{k-1}) - \hat{\boldsymbol{x}}^-(t_k)]^T \tag{4.36c}$$

Measurement Update

A priori estimate of $\hat{\boldsymbol{y}}(t_k)$ shown as $\hat{\boldsymbol{y}}^-(t_k)$ was calculated using

$$\mathcal{Y}_i(t_k|t_{k-1}) = \boldsymbol{H}(\mathcal{X}_i(t_k|t_{k-1})) \quad i = 0, \cdots, 2L \tag{4.37a}$$

$$\hat{\boldsymbol{y}}^-(t_k) = \sum_{i=0}^{2L} W_i^m \mathcal{Y}_i(t_k|t_{k-1}) \tag{4.37b}$$

$$\hat{\boldsymbol{P}}_{\boldsymbol{y}}(t_k) = \boldsymbol{R}(t_k) + \sum_{i=0}^{2L} W_i^c [\mathcal{Y}_i(t_k|t_{k-1}) - \hat{\boldsymbol{y}}^-(t_k)][\mathcal{Y}_i(t_k|t_{k-1}) - \hat{\boldsymbol{y}}^-(t_k)]^T \tag{4.37c}$$

$$\hat{\boldsymbol{P}}_{\boldsymbol{xy}}(t_k) = \sum_{i=0}^{2L} W_i^c [\mathcal{X}_i(t_k|t_{k-1}) - \hat{\boldsymbol{x}}^-(t_k)][\mathcal{Y}_i(t_k|t_{k-1}) - \hat{\boldsymbol{y}}^-(t_k)]^T \tag{4.37d}$$

State Correction

Kalman filter needs a measurement of the system output at time t_k ($\hat{\boldsymbol{y}}(t_k)$) to be incorporated into the filter process by computing an innovation vector as the difference between the measurement of the system output and *a priori* estimate of it ($\hat{\boldsymbol{y}}(t_k) - \hat{\boldsymbol{y}}^-(t_k)$). In this work, it is proposed that this measurement should be provided to the filter by employing a different type of sensor that can estimate the relative orientation of the two frames $\mathcal{F}1$ and $\mathcal{F}2$. Fiber strain sensors as a potential solution were used in this work, and a machine learning algorithm with the sensors' signals as the input and the relative orientation as the output estimated the vector $\hat{\boldsymbol{y}}(t_k)$. *A posteriori* estimate of the state vector $\hat{\boldsymbol{x}}(t_k)$ and covariance matrix $\hat{\boldsymbol{P}}_x(t_k)$ can therefore be calculated as follows [110]

$$\mathcal{K} = \hat{\boldsymbol{P}}_{\boldsymbol{xy}}(t_k)\hat{\boldsymbol{P}}_{\boldsymbol{y}}^{-1}(t_k) \tag{4.38a}$$

$$\hat{\boldsymbol{x}}(t_k) = \hat{\boldsymbol{x}}^{-}(t_k) + \mathcal{K}(\hat{\boldsymbol{y}}(t_k) - \hat{\boldsymbol{y}}^{-}(t_k)) \tag{4.38b}$$

$$\hat{\boldsymbol{P}}_{\boldsymbol{x}}(t_k) = \hat{\boldsymbol{P}}_{\boldsymbol{x}}^{-}(t_k) - \mathcal{K}\hat{\boldsymbol{P}}_{\boldsymbol{y}}(t_k)\mathcal{K}^T \tag{4.38c}$$

Renormalization

The operations that comprise sums of variables and multiplications of variables by a scalar in the UKF process do not preserve the unit norm constraint of rotation quaternions [109]. This leads to the accumulation of error and therefore filter failure. Consequently, different modifications of the UKF were proposed for quaternionic systems to preserve the unit constraint. The simplest solution is the brute-force normalization [109]. After *a posteriori* estimate of the state vector is calculated, this estimation is normalized to satisfy the unit constraint. In this work, brute-force normalization was employed, and the quaternion part of the posterior state estimation was normalized using the following formula

$${}^{\mathcal{F}2}_{\mathcal{F}1}\hat{\bar{q}} = \frac{{}^{\mathcal{F}2}_{\mathcal{F}1}\hat{\bar{q}}}{||{}^{\mathcal{F}2}_{\mathcal{F}1}\hat{\bar{q}}||} \tag{4.39}$$

The term $||{}^{\mathcal{F}2}_{\mathcal{F}1}\hat{\bar{q}}||$ is the norm of the quaternion and defined as

$$||{}^{\mathcal{F}2}_{\mathcal{F}1}\hat{\bar{q}}|| = \sqrt{q_1^2 + q_2^2 + q_3^2 + q_4^2} \tag{4.40}$$

4.4 Experimental Results

4.4.1 Experimental Setup

Despite the joints such as knee and elbow that can be assumed as a hinge joint, trunk, and spheroidal joints, e.g., the ankle and the hip can have free 3-dimensional movements. Strong geometrical constraints can not therefore be used straightforwardly to improve the joint angle estimation for these joints. Accordingly, 3-dimensional complex movements of the trunk were selected to validate the performance of the proposed algorithm. Two Xsens MTw Awinda IMUs(Xsens Technologies B.V.) and the wearable smart garment developed in the previous chapter were employed for data collection. An optical motion capture system(Vicon, Oxford, UK) with two reflective markers sets were used to generate the ground truth relative orientation. Figure 4.2 shows the experimental setup. One IMU was attached to the subjects' C7 spinal vertebra, and the other one was attached to the S1 spinal vertebra. A set of reflective markers was attached to each IMU to calculate the correct orientation of the IMUs. The smart garment consisted of 18 strain sensors that measure the change of the strain pattern in the garment induced by the trunk motion. This garment was designed to measure the 3-dimensional kinematic angles of the trunk with respect to the pelvis using the strain pattern change. The design and testing details of this smart garment was shown in the last chapter. A random forest machine learning regressor algorithm with the raw strain sensors signals and extracted features as the input and the optic-based Euler angles of the relative orientation between the two IMUs as the output was trained and then tested in a 3-fold cross-validation approach to have the estimation required for the proposed data fusion algorithm in this work. Scikit-learn python package was used for conducting this analysis [111].

The conducted experiments comprised 10 participants performing an exhaustive set of uniaxial and multiaxial movements with three different speeds of slow, moderate, and fast. The set of the movements is shown in Table 3.2. In an attempt to investigate the performance of the different algorithms under harsh magnetic disturbances, all data collection experiments were conducted in a biomechanics laboratory with disturbances causing severe distortion in the magnetometer measured earth magnetic field.

Herein, our proposed data fusion algorithm (DF) was contrasted with two other data fusion approaches to assess its performance. The first algorithm was the random forest machine learning algorithm (RF) using only the strain sensors [51], and the second approach was the Xsens built-in Kalman filter (XKF) [112]. In the later approach, the filter was applied to each IMU separately to generate its orientation using an accelerometer, magnetometer, and gyroscope data, and then the relative orientation was calculated. Root Mean

Figure 4.2: The experimental setup used for collecting trunk motion data from IMU units and smart garment with integrated fiber strain sensors.

Squared Error(RMSE) was used as the comparison metrics between the real and estimated trunk Euler angles of roll(flexion movement), pitch(rotation movement), and yaw(lateral bending movement).

4.4.2 Experimental Demonstration and Discussion

Table 4.1 represents the performance of the three algorithms for all participants in each movement averaged over three speeds. Factors that determine the accuracy of orientation estimation are movement environment and movement characteristics, including movement speed, complexity, range, and period [53, 70, 71]. The data collection was therefore performed in an environment with severe magnetic disturbance and comprised a series of simple to complex movements with three different speeds. As it can be seen in Table 4.1, the magnetic disturbance has affected the XKF performance so that in the rotation movement,

Table 4.1: Comparison of the movement tracking accuracy using 3 algorithms of random forest (RF), XSens Kalam filter (XKF), and the proposed data fusion algorithm (DF)

		RMSE		
		XKF	RF	DF
R	roll	1.50	3.23	1.21
	pitch	5.72	1.66	1.70
	yaw	4.17	2.45	1.60
LB	roll	1.26	3.65	1.42
	pitch	5.46	3.60	1.35
	yaw	3.28	1.94	1.59
F	roll	1.45	3.08	2.45
	pitch	4.41	4.16	0.62
	yaw	4.45	3.13	0.92
S	roll	3.33	2.39	2.89
	pitch	3.24	1.17	1.35
	yaw	2.43	2.12	1.56
FLB	roll	1.53	4.27	2.38
	pitch	3.78	4.08	2.26
	yaw	3.45	3.12	1.79
FR	roll	2.53	4.6	2.15
	pitch	4.03	4.36	1.86
	yaw	4.62	3.02	1.36
LBR	roll	1.99	4.29	2.06
	pitch	3.90	4.26	1.62
	yaw	4.22	3.38	2.08
RM	roll	3.78	5.13	3.07
	pitch	5.57	4.90	3.01
	yaw	6.97	4.48	2.93
Mean	roll	2.17	3.83	2.20
	pitch	4.52	3.52	1.72
	yaw	4.20	2.96	1.73

the XKF has 5.72° error in estimating the rotation angle. It has been shown that the trunk rotation angle is the most challenging angle to estimate using inertial sensors [104]. However, both DF and RF had acceptable errors below 2° in estimating the trunk rotation angle. The XKF significant higher error in rotation angle estimation is because of the susceptibility of the magnetometers to the environment magnetic disturbances, which limits the application of this filter in such condition.

Comparing movement conditions in Table 4.1, it is clear that as the movement becomes more complex, the RF error level increases, ranging from 2° to 5°. This result shows that movement complexity also affects the angle estimation in the RF algorithm. For the XKF algorithm, errors in different movement conditions range from 1.50° to 6.97° with the maximum error in random movements. Our proposed data fusion technique has a constant error level of below 3° between the simple and complex movements while most of the conditions have errors less than 2°. This result indicates that the data fusion technique has eliminated the movement dependency of angle estimation. This is an essential result for developing reliable wearable motion tracking systems that can be used for *in situ* motion tracking.

Averaging over all movement conditions, the recommended data fusion algorithm estimated trunk flexion, rotation, and lateral bending with errors of 2.20°, 1.72°, and 1.73° respectively. It is recommended that an error of 2° and less is acceptable for the clinical application of estimated kinematic angles with no further consideration [113]. The angle estimation of the DF is well under this limit in rotation and lateral bending angles and slightly higher in the flexion movement. Average error of both XKF and RF algorithms is higher than 2°, which means these results require more detailed consideration while interpreting the estimated kinematic angles. Despite the complexity of movements, the DF algorithm yielded a promising level of error in estimation of the relative orientation between the two IMUs, which falls under the recommended limit and is well comparable with the previous studies in IMU-based trunk motion tracking [104, 114].

Figure 4.3 illustrates the angle estimation of all the algorithms in a random movement condition. Random movement is most likely how the user would use any wearable motion tracking system. Including this type of movement is therefore a crucial testing for examining

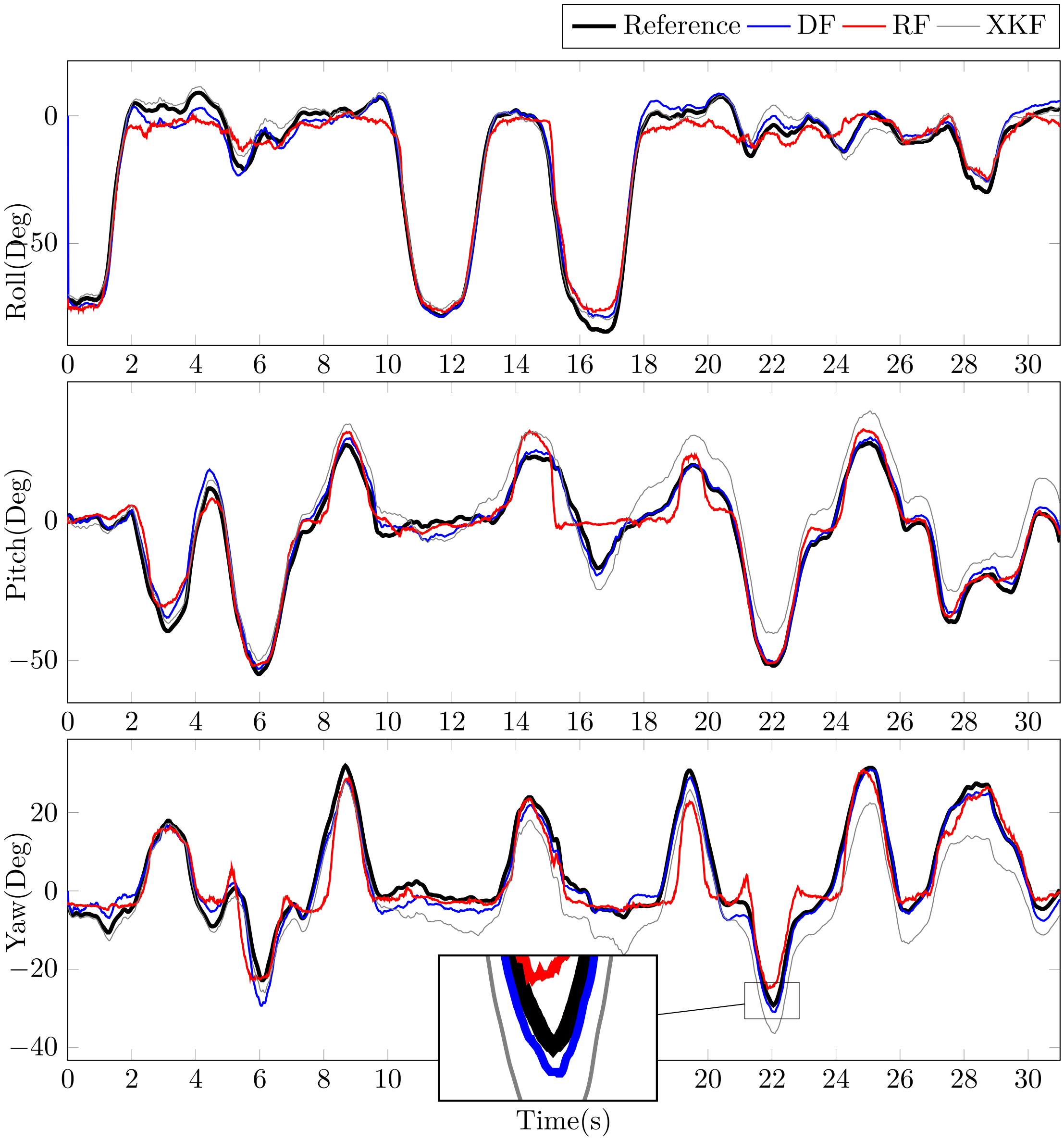

Figure 4.3: Comparison between the orientation estimation of the 3 different algorithms with the reference values.

the performance of wearable motion tracking systems. As it can be seen in Figure 4.3, the XKF filter estimation drifts from the real value over time whereas the RF algorithm estimation follow the reference pattern with no drift. However, in a complicated movement similar to this random pattern, RF error increases significantly. Removing the magnetometer and fusing the strain sensors and gyroscopes data in our proposed algorithm improved the basic RF estimation so that the roll, pitch, and yaw error decreased from 5.13°, 4.90°, and

4.48° to 3.07°, 3.01°, and 2.93° respectively. This data fusion algorithm is a novel solution for fusing data from different sensor types that have not previously been used in such a unified manner.

In the proposed data fusion algorithm, both IMU sensors data were combined in one UKF filter. Using the XKF for relative orientation estimation, the filter is applied to each IMU unit separately, and then having the two absolute orientations, the relative orientation between the two IMUs can be calculated. It was shown in the literature that applying the filter to each IMU; it is possible to achieve a constant acceptable error of less than 1° for each IMU absolute roll and pitch angles estimation [63]. However, heading estimation has been a challenge because of the magnetometer susceptibility to environmental magnetic disturbances. Different solutions such as magnetometer-free filters, magnetic mapping of the environment prior to data collection and double step filters have been suggested in the literature as possible solutions [63, 102, 104]. Yaw angle drift is however still present using these methods and affects the relative orientation calculation. Figure 4.4 shows the error drift of each two IMUs and the corresponding relative orientation error drift for the 3 Euler angles. It can be seen that roll and pitch angles have constant minimal errors, but yaw error drifts over time. When calculating the relative orientation, the yaw errors of the two IMUs are projected on the relative roll and pitch angles. Consequently, although each IMU has accurate roll and pitch angles, relative orientation roll and pitch angles are not accurate due to the absolute yaw errors of the two IMUs. In the proposed algorithm, magnetometer and accelerometer are replaced with strain sensors. Strain sensors are not accurate enough for independent use in complex body movements, but they do not suffer from the drift problem, and therefore DF algorithm eliminated the drift and outperformed the typical IMU sensor data fusion algorithms.

4.5 Summary

A novel data fusion algorithm was developed and tested in a study with 10 participants performing 1-dimensional to 3-dimensional trunk movements. Although the algorithm was tested for trunk movements, it can be employed for any joints. This algorithm uses the two

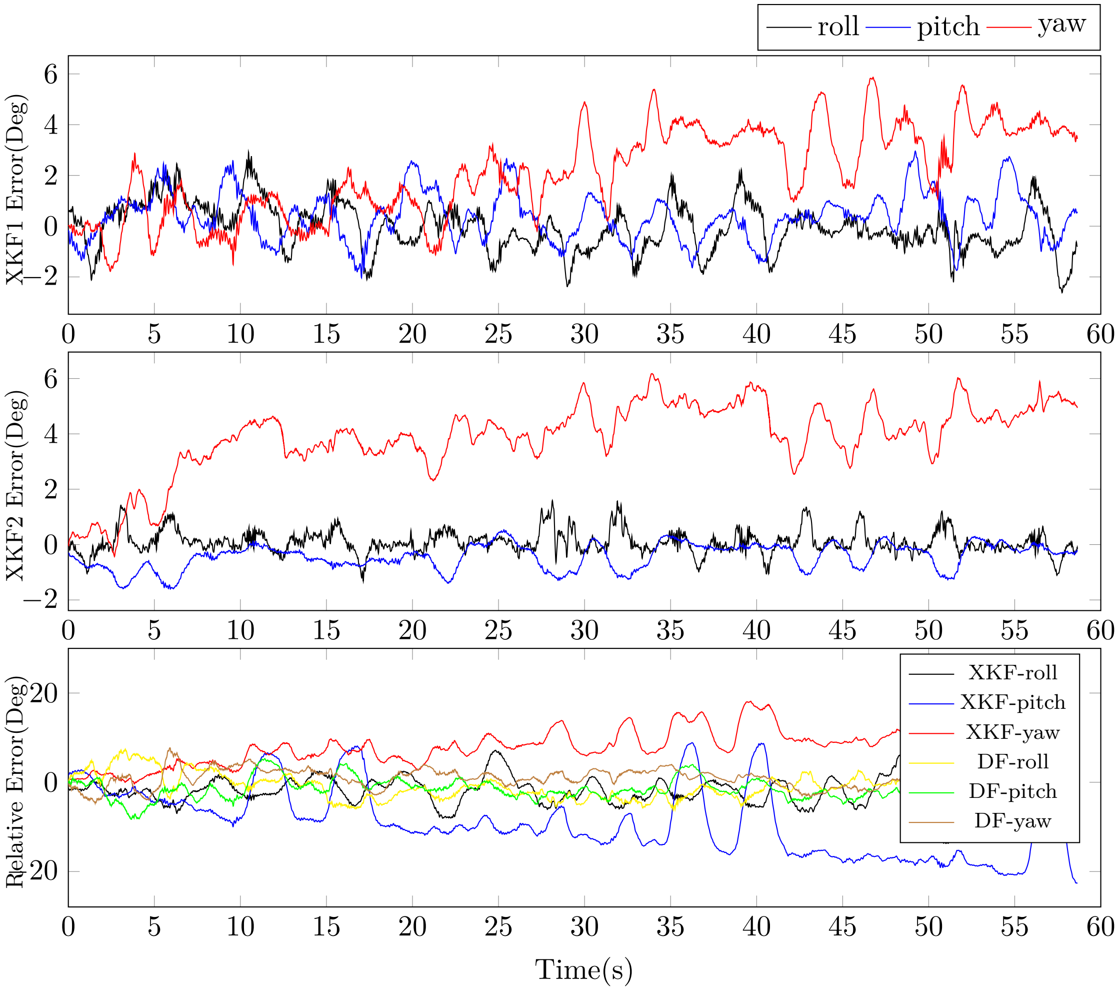

Figure 4.4: The roll, pitch, and yaw absolute error of the XKF algorithm in IMU 1 and 2 and the XKF-based relative orientation

gyroscope and strain sensors data and provides an estimation of the relative orientation between the two dynamic reference frames of the gyroscopes. Averaged over all participants, the algorithm estimated trunk flexion, rotation, and lateral bending with 2.20°, 1.72°, and 1.73° error which is a superior level of error considering the complexity of the conducted movements. Contrasting with the common XKF and the random forest algorithm, the proposed data fusion algorithm had an excellent improved performance where its errors were significantly lower than the two other algorithms. This suggests the inertial and strain-based data fusion as a solution for developing reliable, accurate wearable motion tracking systems that can be used for indoor and outdoor applications. This chapter addressed the second objective of this thesis for the overall wearable motion tracking performance improvement.

Chapter 5

Conclusion

In this thesis, a wearable motion tracking system employing thread-like strain sensors integrated inside a garment was developed for measuring trunk 3-dimensional kinematic angles. Using a random forest regressor, this system detected trunk flexion, rotation, and lateral bending angles with 4.26°, 3.52°, and 3.4° error, respectively. This showed the feasibility of smart textile systems for measuring kinematic data of multiaxial movements. This system can be useful for developing alternatives for typical wearable motion capture systems using only IMU sensors. However, this study demonstrated that using fiber strain sensors for wearable motion tracking has limitations as the accuracy of the motion tracking was different between movement types. The algorithm showed high accuracy in planar movements tracking the reference angle accurately, whereas in 3-dimensional movements, the accuracy of movement tracking dropped down. The results of this study addressed the objective 1 of this thesis in developing and testing a strain-based motion tracking system. In the next study, the performance of this developed system was further improved by developing a data fusion algorithm for using the gyroscopes data for motion tracking.

Chapter 4 addressed the second objective of the thesis by proposing a novel data fusion algorithm for relative orientation estimation between two dynamic coordinate frames with nonzero angular velocities (local coordinated frames of IMUs). It was proposed that the conventional approach of calculating the absolute orientation of each IMU unit with respect to an inertial reference frame with zero angular velocity and further relative orientation calculation between the two units using these absolute orientations can be replaced with one unscented Kalman filter applied directly to the relative orientation estimation.

This approach needs a measurement of the relative orientation, and since accelerometer and magnetometer can only provide attitude measurements with respect to the inertial reference frame, it was suggested that other wearable sensors such as fiber strain sensors could be used for generating this relative orientation. Consequently, this study suggested a data fusion algorithm for fusing two gyroscopes data with a different type of sensor such as fiber strain sensors capable of estimating the relative orientation. As required for the time update step of the UKF, the dynamic reference frames relative orientation kinematic equation was derived and further discretized to be used as the state-space model of the system. Using this state-space model and the measurement updates generated from strain sensors signals, a UKF was developed. To investigate the performance of the proposed algorithm, a study with 10 participants performing 3-dimensional trunk movements was conducted, and the proposed filter was applied to the neck and sacrum gyroscopes and a set of 18 strain sensors data. The results of this filter were contrasted with other conventional filters, and the proposed algorithm outperformed the other approaches in estimating trunk orientation angles. Trunk movements were selected for this experiment as geometrical constraints can not easily be used for filter performance improvement for the trunk. In addition, 3-dimensional movements were included in the study as these movements will most likely happen in daily living. The proposed solution estimated trunk flexion, rotation, and lateral bending with 2.20°, 1.72°, and 1.73° error, which is accurate enough to be used for clinical applications with no further consideration.

IMUs and Strain sensors are the two prominent wearable sensors used for unconstrained monitoring of activities. However, they both have limitations that have hindered their widespread application. The overall conclusion of this thesis is that due to the limitations of the inertial-based and strain-based motion tracking approaches, developing accurate, reliable wearable solutions for unconstrained indoor and outdoor motion tracking would therefore be feasible by employing the two types of sensor together so that they compensate for each other drawbacks. This thesis further suggests an algorithm for data fusion of the two types and demonstrates that the individual application of each wearable sensor would suffer from limitations and has lower accuracy in movement tracking, whereas the data fusion algorithm outperforms both individual algorithms.

Bibliography

[1] W. S. Marras, R. G. Cutlip, S. E. Burt, and T. R. Waters, "National occupational research agenda (nora) future directions in occupational musculoskeletal disorder health research," *Applied ergonomics*, vol. 40, no. 1, pp. 15–22, 2009.

[2] M. Allegri, S. Montella, F. Salici, A. Valente, M. Marchesini, C. Compagnone, M. Baciarello, M. E. Manferdini, and G. Fanelli, "Mechanisms of low back pain: a guide for diagnosis and therapy," *F1000Research*, vol. 5, p. 1530, 2016.

[3] E. Papi, W. S. Koh, and A. H. McGregor, "Wearable technology for spine movement assessment: A systematic review," *Journal of biomechanics*, vol. 64, pp. 186–197, 2017.

[4] E. Clays, D. De Bacquer, F. Leynen, M. Kornitzer, F. Kittel, and G. De Backer, "The impact of psychosocial factors on low back pain: longitudinal results from the belstress study," *Spine*, vol. 32, no. 2, pp. 262–268, 2007.

[5] B. N. Craig, J. J. Congleton, E. Beier, C. J. Kerk, A. A. Amendola, and W. G. Gaines, "Occupational risk factors and back injury," *International Journal of Occupational Safety and Ergonomics*, vol. 19, no. 3, pp. 335–345, 2013.

[6] X. Shan, X. Ning, Z. Chen, M. Ding, W. Shi, and S. Yang, "Low back pain development response to sustained trunk axial twisting," *European Spine Journal*, vol. 22, no. 9, pp. 1972–1978, 2013.

[7] D. C. Ribeiro, G. Sole, J. H. Abbott, and S. Milosavljevic, "Cumulative postural exposure measured by a novel device: a preliminary study," *Ergonomics*, vol. 54, no. 9, pp. 858–865, 2011.

[8] D. C. Ribeiro, D. Aldabe, J. H. Abbott, G. Sole, and S. Milosavljevic, "Dose–response relationship between work-related cumulative postural exposure and low back pain: a systematic review," *Annals of occupational hygiene*, vol. 56, no. 6, pp. 684–696, 2012.

[9] M. Dreischarf, E. Pries, M. Bashkuev, M. Putzier, and H. Schmidt, "Differences between clinical "snap-shot" and "real-life" assessments of lumbar spine alignment and motion–what is the "real" lumbar lordosis of a human being?" *Journal of biomechanics*, vol. 49, no. 5, pp. 638–644, 2016.

[10] J. Mendes Jr, M. Vieira, M. Pires, and S. Stevan Jr, "Sensor fusion and smart sensor in sports and biomedical applications," *Sensors*, vol. 16, no. 10, p. 1569, 2016.

[11] H. Allen, A. R. Coggan, and S. McGregor, *Training and racing with a power meter.* VeloPress, 2019.

[12] P. Siirtola, P. Laurinen, J. Röning, and H. Kinnunen, “Efficient accelerometer-based swimming exercise tracking,” in *2011 IEEE Symposium on Computational Intelligence and Data Mining (CIDM).* IEEE, 2011, pp. 156–161.

[13] R. Needham, J. Stebbins, and N. Chockalingam, “Three-dimensional kinematics of the lumbar spine during gait using marker-based systems: a systematic review,” *Journal of medical engineering & technology*, vol. 40, no. 4, pp. 172–185, 2016.

[14] S. Patel, H. Park, P. Bonato, L. Chan, and M. Rodgers, “A review of wearable sensors and systems with application in rehabilitation,” *Journal of neuroengineering and rehabilitation*, vol. 9, no. 1, p. 21, 2012.

[15] C. Strohrmann, H. Harms, C. Kappeler-Setz, and G. Troster, “Monitoring kinematic changes with fatigue in running using body-worn sensors,” *IEEE transactions on information technology in biomedicine*, vol. 16, no. 5, pp. 983–990, 2012.

[16] M. Ermes, J. Pärkkä, J. Mäntyjärvi, and I. Korhonen, “Detection of daily activities and sports with wearable sensors in controlled and uncontrolled conditions,” *IEEE transactions on information technology in biomedicine*, vol. 12, no. 1, pp. 20–26, 2008.

[17] G. Appelboom, E. Camacho, M. E. Abraham, S. S. Bruce, E. L. Dumont, B. E. Zacharia, R. D’Amico, J. Slomian, J. Y. Reginster, O. Bruyère *et al.*, “Smart wearable body sensors for patient self-assessment and monitoring,” *Archives of public health*, vol. 72, no. 1, p. 28, 2014.

[18] P. Bonato, “Wearable sensors and systems,” *IEEE Engineering in Medicine and Biology Magazine*, pp. 25–36, 2010.

[19] P. Castillejo, J.-F. Martinez, J. Rodriguez-Molina, and A. Cuerva, “Integration of wearable devices in a wireless sensor network for an e-health application,” *IEEE Wireless Communications*, vol. 20, no. 4, pp. 38–49, 2013.

[20] B. Mariani, M. C. Jiménez, F. J. Vingerhoets, and K. Aminian, “On-shoe wearable sensors for gait and turning assessment of patients with parkinson’s disease,” *IEEE transactions on biomedical engineering*, vol. 60, no. 1, pp. 155–158, 2012.

[21] B.-R. Chen, S. Patel, T. Buckley, R. Rednic, D. J. McClure, L. Shih, D. Tarsy, M. Welsh, and P. Bonato, “A web-based system for home monitoring of patients with parkinson’s disease using wearable sensors,” *IEEE Transactions on Biomedical Engineering*, vol. 58, no. 3, pp. 831–836, 2010.

[22] O. Aziz and S. N. Robinovitch, “An analysis of the accuracy of wearable sensors for classifying the causes of falls in humans,” *IEEE transactions on neural systems and rehabilitation engineering*, vol. 19, no. 6, pp. 670–676, 2011.

[23] T. Shany, S. J. Redmond, M. R. Narayanan, and N. H. Lovell, “Sensors-based wearable systems for monitoring of human movement and falls,” *IEEE Sensors Journal*, vol. 12, no. 3, pp. 658–670, 2011.

[24] U. Kramer, S. Kipervasser, A. Shlitner, and R. Kuzniecky, “A novel portable seizure detection alarm system: preliminary results,” *Journal of Clinical Neurophysiology*, vol. 28, no. 1, pp. 36–38, 2011.

[25] O. Amft and G. Tröster, "Recognition of dietary activity events using on-body sensors," *Artificial intelligence in medicine*, vol. 42, no. 2, pp. 121–136, 2008.

[26] J. M. Jakicic, K. K. Davis, R. J. Rogers, W. C. King, M. D. Marcus, D. Helsel, A. D. Rickman, A. S. Wahed, and S. H. Belle, "Effect of wearable technology combined with a lifestyle intervention on long-term weight loss: the idea randomized clinical trial," *Jama*, vol. 316, no. 11, pp. 1161–1171, 2016.

[27] A. Ejupi and C. Menon, "Detection of talking in respiratory signals: A feasibility study using machine learning and wearable textile-based sensors," *Sensors*, vol. 18, no. 8, p. 2474, 2018.

[28] D. J. Cook, A. Crandall, G. Singla, and B. Thomas, "Detection of social interaction in smart spaces," *Cybernetics and Systems: An International Journal*, vol. 41, no. 2, pp. 90–104, 2010.

[29] N. Eagle and A. S. Pentland, "Reality mining: sensing complex social systems," *Personal and ubiquitous computing*, vol. 10, no. 4, pp. 255–268, 2006.

[30] B. Ainsworth, L. Cahalin, M. Buman, and R. Ross, "The current state of physical activity assessment tools," *Progress in cardiovascular diseases*, vol. 57, no. 4, pp. 387–395, 2015.

[31] L. E. Dunne, P. Walsh, B. Smyth, and B. Caulfield, "Design and evaluation of a wearable optical sensor for monitoring seated spinal posture," in *2006 10th IEEE International Symposium on Wearable Computers*. IEEE, 2006, pp. 65–68.

[32] W. Marras, F. Fathallah, R. Miller, S. Davis, and G. Mirka, "Accuracy of a three-dimensional lumbar motion monitor for recording dynamic trunk motion characteristics," *International Journal of Industrial Ergonomics*, vol. 9, no. 1, pp. 75–87, 1992.

[33] R. Ellegast and J. Kupfer, "Portable posture and motion measuring system for use in ergonomic field analysis," *Ergonomic software tools in product and workplace design*, vol. 47, p. 54, 2000.

[34] W. S. Marras, K. G. Davis, B. C. Kirking, and P. K. Bertsche, "A comprehensive analysis of low-back disorder risk and spinal loading during the transferring and repositioning of patients using different techniques," *Ergonomics*, vol. 42, no. 7, pp. 904–926, 1999.

[35] S. Freitag, R. Ellegast, M. Dulon, and A. Nienhaus, "Quantitative measurement of stressful trunk postures in nursing professions," *Annals of Occupational Hygiene*, vol. 51, no. 4, pp. 385–395, 2007.

[36] R. Ellegast, I. Hermanns, and C. Schiefer, "Workload assessment in field using the ambulatory cuela system," in *International Conference on Digital Human Modeling*. Springer, 2009, pp. 221–226.

[37] A. Plamondon, A. Delisle, C. Larue, D. Brouillette, D. McFadden, P. Desjardins, and C. Larivière, "Evaluation of a hybrid system for three-dimensional measurement of trunk posture in motion," *Applied Ergonomics*, vol. 38, no. 6, pp. 697–712, 2007.

[38] M. C. Schall Jr, N. B. Fethke, H. Chen, and F. Gerr, "A comparison of instrumentation methods to estimate thoracolumbar motion in field-based occupational studies," *Applied ergonomics*, vol. 48, pp. 224–231, 2015.

[39] J. Bell and M. Stigant, "Development of a fibre optic goniometer system to measure lumbar and hip movement to detect activities and their lumbar postures," *Journal of medical engineering & technology*, vol. 31, no. 5, pp. 361–366, 2007.

[40] E. Sardini, M. Serpelloni, and V. Pasqui, "Daylong sitting posture measurement with a new wearable system for at home body movement monitoring," in *2015 IEEE International Instrumentation and Measurement Technology Conference (I2MTC) Proceedings.* IEEE, 2015, pp. 652–657.

[41] T. Consmüller, A. Rohlmann, D. Weinland, C. Druschel, G. N. Duda, and W. R. Taylor, "Comparative evaluation of a novel measurement tool to assess lumbar spine posture and range of motion," *European Spine Journal*, vol. 21, no. 11, pp. 2170–2180, 2012.

[42] A. Yamamoto, H. Nakamoto, T. Yamaji, H. Ootaka, Y. Bessho, R. Nakamura, and R. Ono, "Method for measuring tri-axial lumbar motion angles using wearable sheet stretch sensors," *PloS one*, vol. 12, no. 10, p. e0183651, 2017.

[43] K. O'Sullivan, S. Verschueren, S. Pans, D. Smets, K. Dekelver, and W. Dankaerts, "Validation of a novel spinal posture monitor: comparison with digital videofluoroscopy," *European Spine Journal*, vol. 21, no. 12, pp. 2633–2639, 2012.

[44] A. Toney, "A novel method for joint motion sensing on a wearable computer." in *iswc*, 1998, pp. 158–159.

[45] A. Bhattacharya, J. Warren, J. Teuschler, M. Dimov, M. Medvedovic, and G. Lemasters, "Development and evaluation of a microprocessor-based ergonomic dosimeter for evaluating carpentry tasks," *Applied ergonomics*, vol. 30, no. 6, pp. 543–553, 1999.

[46] S. Kim and M. A. Nussbaum, "Performance evaluation of a wearable inertial motion capture system for capturing physical exposures during manual material handling tasks," *Ergonomics*, vol. 56, no. 2, pp. 314–326, 2013.

[47] L. Simpson, M. M. Maharaj, and R. J. Mobbs, "The role of wearables in spinal posture analysis: a systematic review," *BMC musculoskeletal disorders*, vol. 20, no. 1, p. 55, 2019.

[48] A. Tognetti, F. Lorussi, R. Bartalesi, S. Quaglini, M. Tesconi, G. Zupone, and D. De Rossi, "Wearable kinesthetic system for capturing and classifying upper limb gesture in post-stroke rehabilitation," *Journal of NeuroEngineering and Rehabilitation*, vol. 2, no. 1, p. 8, 2005.

[49] M. I. Mokhlespour Esfahani, S. Taghinezhad, V. Mottaghitalab, R. Narimani, and M. Parnianpour, "Novel printed body worn sensor for measuring the human movement orientation," *Sensor Review*, vol. 36, no. 3, pp. 321–331, 2016.

[50] A. Rezaei, A. Ejupi, M. Gholami, A. Ferrone, and C. Menon, “Preliminary investigation of textile-based strain sensors for the detection of human gait phases using machine learning,” in *2018 7th IEEE International Conference on Biomedical Robotics and Biomechatronics (Biorob).* IEEE, 2018, pp. 563–568.

[51] A. Rezaei, T. J. Cuthbert, M. Gholami, and C. Menon, “Application-based production and testing of a core–sheath fiber strain sensor for wearable electronics: Feasibility study of using the sensors in measuring tri-axial trunk motion angles,” *Sensors*, vol. 19, no. 19, p. 4288, 2019.

[52] M. Mokhlespour Esfahani and M. Nussbaum, “Preferred placement and usability of a smart textile system vs. inertial measurement units for activity monitoring,” *Sensors*, vol. 18, no. 8, p. 2501, 2018.

[53] K. Lebel, P. Boissy, M. Hamel, and C. Duval, “Inertial measures of motion for clinical biomechanics: comparative assessment of accuracy under controlled conditions-effect of velocity,” *PloS one*, vol. 8, no. 11, p. e79945, 2013.

[54] P. B. Shull, W. Jirattigalachote, M. A. Hunt, M. R. Cutkosky, and S. L. Delp, “Quantified self and human movement: a review on the clinical impact of wearable sensing and feedback for gait analysis and intervention,” *Gait & posture*, vol. 40, no. 1, pp. 11–19, 2014.

[55] R. Gravina, P. Alinia, H. Ghasemzadeh, and G. Fortino, “Multi-sensor fusion in body sensor networks: State-of-the-art and research challenges,” *Information Fusion*, vol. 35, pp. 68–80, 2017.

[56] M. Iosa, P. Picerno, S. Paolucci, and G. Morone, “Wearable inertial sensors for human movement analysis,” *Expert review of medical devices*, vol. 13, no. 7, pp. 641–659, 2016.

[57] A. M. Sabatini, “Estimating three-dimensional orientation of human body parts by inertial/magnetic sensing,” *Sensors*, vol. 11, no. 2, pp. 1489–1525, 2011.

[58] A. Filippeschi, N. Schmitz, M. Miezal, G. Bleser, E. Ruffaldi, and D. Stricker, “Survey of motion tracking methods based on inertial sensors: A focus on upper limb human motion,” *Sensors*, vol. 17, no. 6, p. 1257, 2017.

[59] G. F. Welch, “History: The use of the kalman filter for human motion tracking in virtual reality,” *Presence: Teleoperators and Virtual Environments*, vol. 18, no. 1, pp. 72–91, 2009.

[60] R. Van Der Merwe, E. Wan, and S. Julier, “Sigma-point kalman filters for nonlinear estimation and sensor-fusion: Applications to integrated navigation,” in *AIAA Guidance, Navigation, and Control Conference and Exhibit*, 2004, p. 5120.

[61] R. E. Kalman, “A new approach to linear filtering and prediction problems,” *Journal of basic Engineering*, vol. 82, no. 1, pp. 35–45, 1960.

[62] E. A. Wan and R. V. D. Merwe, “The unscented Kalman filter for nonlinear estimation,” in *Proceedings of the IEEE 2000 Adaptive Systems for Signal Processing, Communications, and Control Symposium (Cat. No.00EX373)*, Oct. 2000, pp. 153–158.

[63] X. Tong, Y. Su, Z. Li, C. Si, G. Han, J. Ning, and F. Yang, "A double-step unscented kalman filter and hmm-based zero velocity update for pedestrian dead reckoning using mems sensors," *IEEE Transactions on Industrial Electronics*, vol. 67, no. 1, pp. 581–591, 2019.

[64] Y. Tian, H. Wei, and J. Tan, "An adaptive-gain complementary filter for real-time human motion tracking with marg sensors in free-living environments," *IEEE Transactions on Neural Systems and Rehabilitation Engineering*, vol. 21, no. 2, pp. 254–264, 2012.

[65] H. D. Black, "A passive system for determining the attitude of a satellite," *AIAA journal*, vol. 2, no. 7, pp. 1350–1351, 1964.

[66] O. Dehzangi, M. Taherisadr, and R. ChangalVala, "Imu-based gait recognition using convolutional neural networks and multi-sensor fusion," *Sensors*, vol. 17, no. 12, p. 2735, 2017.

[67] A. Tafazzol, N. Arjmand, A. Shirazi-Adl, and M. Parnianpour, "Lumbopelvic rhythm during forward and backward sagittal trunk rotations: combined in vivo measurement with inertial tracking device and biomechanical modeling," *Clinical Biomechanics*, vol. 29, no. 1, pp. 7–13, 2014.

[68] M. Hajibozorgi and N. Arjmand, "Sagittal range of motion of the thoracic spine using inertial tracking device and effect of measurement errors on model predictions," *Journal of biomechanics*, vol. 49, no. 6, pp. 913–918, 2016.

[69] P. Intolo, A. B. Carman, S. Milosavljevic, J. H. Abbott, and G. D. Baxter, "The spineangel®: Examining the validity and reliability of a novel clinical device for monitoring trunk motion," *Manual Therapy*, vol. 15, no. 2, pp. 160–166, 2010.

[70] X. Robert-Lachaine, H. Mecheri, C. Larue, and A. Plamondon, "Validation of inertial measurement units with an optoelectronic system for whole-body motion analysis," *Medical & biological engineering & computing*, vol. 55, no. 4, pp. 609–619, 2017.

[71] K. Lebel, P. Boissy, M. Hamel, and C. Duval, "Inertial measures of motion for clinical biomechanics: Comparative assessment of accuracy under controlled conditions–changes in accuracy over time," *PloS one*, vol. 10, no. 3, p. e0118361, 2015.

[72] A. Godwin, M. Agnew, and J. Stevenson, "Accuracy of inertial motion sensors in static, quasistatic, and complex dynamic motion," *Journal of biomechanical engineering*, vol. 131, no. 11, p. 114501, 2009.

[73] M. Brodie, A. Walmsley, and W. Page, "Dynamic accuracy of inertial measurement units during simple pendulum motion," *Computer methods in biomechanics and biomedical engineering*, vol. 11, no. 3, pp. 235–242, 2008.

[74] A. Samadani, A. Lee, and D. Kulić, "A spinal motion measurement protocol utilizing inertial sensors without magnetometers," in *2018 40th Annual International Conference of the IEEE Engineering in Medicine and Biology Society (EMBC)*. IEEE, 2018, pp. 1–4.

[75] T.-H. Ha, K. Saber-Sheikh, A. P. Moore, and M. P. Jones, "Measurement of lumbar spine range of movement and coupled motion using inertial sensors–a protocol validity study," *Manual therapy*, vol. 18, no. 1, pp. 87–91, 2013.

[76] C. Bauer, F. Rast, M. Ernst, J. Kool, S. Oetiker, S. Rissanen, J. Suni, and M. Kankaanpää, "Concurrent validity and reliability of a novel wireless inertial measurement system to assess trunk movement," *Journal of Electromyography and Kinesiology*, vol. 25, no. 5, pp. 782–790, 2015.

[77] M. Gholami, A. Ejupi, A. Rezaei, A. Ferrone, and C. Menon, "Estimation of knee joint angle using a fabric-based strain sensor and machine learning: A preliminary investigation," in *2018 7th IEEE International Conference on Biomedical Robotics and Biomechatronics (Biorob)*. IEEE, 2018, pp. 589–594.

[78] C. Mattmann, O. Amft, H. Harms, G. Troster, and F. Clemens, "Recognizing upper body postures using textile strain sensors," in *2007 11th IEEE international symposium on wearable computers*. IEEE, 2007, pp. 29–36.

[79] M. I. Mokhlespour Esfahani and M. A. Nussbaum, "A"smart"undershirt for tracking upper body motions: Task classification and angle estimation," *IEEE Sensors Journal*, vol. 18, pp. 7650–7658, 2018.

[80] M. Mokhlespour Esfahani and M. Nussbaum, "Classifying diverse physical activities using "smart garments"," *Sensors*, vol. 19, no. 14, p. 3133, 2019.

[81] M. Mokhlespour Esfahani, O. Zobeiri, B. Moshiri, R. Narimani, M. Mehravar, E. Rashedi, and M. Parnianpour, "Trunk motion system (tms) using printed body worn sensor (bws) via data fusion approach," *Sensors*, vol. 17, no. 1, p. 112, 2017.

[82] A. Liaw, M. Wiener *et al.*, "Classification and regression by randomforest," *R news*, vol. 2, no. 3, pp. 18–22, 2002.

[83] S. J. Russell and P. Norvig, *Artificial intelligence: a modern approach*. Malaysia; Pearson Education Limited,, 2016.

[84] I. Goodfellow, Y. Bengio, and A. Courville, *Deep learning*. MIT press, 2016.

[85] A. Ejupi, A. Ferrone, and C. Menon, "Quantification of textile-based stretch sensors using machine learning: An exploratory study," in *2018 7th IEEE International Conference on Biomedical Robotics and Biomechatronics (Biorob)*. IEEE, 2018, pp. 254–259.

[86] E. Papi, I. Spulber, M. Kotti, P. Georgiou, and A. H. McGregor, "Smart sensing system for combined activity classification and estimation of knee range of motion," *IEEE Sensors Journal*, vol. 15, no. 10, pp. 5535–5544, 2015.

[87] L. Breiman, "Random forests," *Machine learning*, vol. 45, no. 1, pp. 5–32, 2001.

[88] B. D. Fulcher and N. S. Jones, "Highly comparative feature-based time-series classification," *IEEE Transactions on Knowledge and Data Engineering*, vol. 26, no. 12, pp. 3026–3037, 2014.

[89] R. Bartalesi, F. Lorussi, D. De Rossi, M. Tesconi, and A. Tognetti, “Wearable monitoring of lumbar spine curvature by inertial and e-textile sensory fusion,” in *2010 Annual International Conference of the IEEE Engineering in Medicine and Biology*. IEEE, 2010, pp. 6373–6376.

[90] A. Tognetti, F. Lorussi, N. Carbonaro, and D. De Rossi, “Wearable goniometer and accelerometer sensory fusion for knee joint angle measurement in daily life,” *Sensors*, vol. 15, no. 11, pp. 28 435–28 455, 2015.

[91] F. Lorussi, N. Carbonaro, D. De Rossi, and A. Tognetti, “A bi-articular model for scapular-humeral rhythm reconstruction through data from wearable sensors,” *Journal of neuroengineering and rehabilitation*, vol. 13, no. 1, p. 40, 2016.

[92] C. Mattmann, “Body posture detection using strain sensitive clothing,” Ph.D. dissertation, ETH Zurich, 2008.

[93] T. Consmüller, A. Rohlmann, D. Weinland, H. Schmidt, T. Zippelius, G. N. Duda, and W. R. Taylor, “Automatic distinction of upper body motions in the main anatomical planes,” *Medical engineering & physics*, vol. 36, no. 4, pp. 516–521, 2014.

[94] C. Mattmann, F. Clemens, and G. Tröster, “Sensor for measuring strain in textile,” *Sensors*, vol. 8, no. 6, pp. 3719–3732, 2008.

[95] P. Tormene, M. Bartolo, A. M. De Nunzio, F. Fecchio, S. Quaglini, C. Tassorelli, and G. Sandrini, “Estimation of human trunk movements by wearable strain sensors and improvement of sensor’s placement on intelligent biomedical clothes,” *Biomedical engineering online*, vol. 11, no. 1, p. 95, 2012.

[96] M. I. Mokhlespour Esfahani, M. A. Nussbaum, and Z. Kong, “Using a smart textile system for classifying occupational manual material handling tasks: evidence from lab-based simulations,” *Ergonomics*, vol. 62, no. 6, pp. 823–833, 2019.

[97] P. Merriaux, Y. Dupuis, R. Boutteau, P. Vasseur, and X. Savatier, “A study of vicon system positioning performance,” *Sensors*, vol. 17, no. 7, p. 1591, 2017.

[98] S. Bersch, D. Azzi, R. Khusainov, I. Achumba, and J. Ries, “Sensor data acquisition and processing parameters for human activity classification,” *Sensors*, vol. 14, no. 3, pp. 4239–4270, 2014.

[99] F. Pedregosa, G. Varoquaux, A. Gramfort, V. Michel, B. Thirion, O. Grisel, M. Blondel, P. Prettenhofer, R. Weiss, V. Dubourg *et al.*, “Scikit-learn: Machine learning in python,” *Journal of machine learning research*, vol. 12, no. Oct, pp. 2825–2830, 2011.

[100] A. I. Cuesta-Vargas, A. Galán-Mercant, and J. M. Williams, “The use of inertial sensors system for human motion analysis,” *Physical Therapy Reviews*, vol. 15, no. 6, pp. 462–473, 2010.

[101] M. C. Schall Jr, N. B. Fethke, H. Chen, S. Oyama, and D. I. Douphrate, “Accuracy and repeatability of an inertial measurement unit system for field-based occupational studies,” *Ergonomics*, vol. 59, no. 4, pp. 591–602, 2016.

[102] W. De Vries, H. Veeger, C. Baten, and F. Van Der Helm, “Magnetic distortion in motion labs, implications for validating inertial magnetic sensors,” *Gait & posture*, vol. 29, no. 4, pp. 535–541, 2009.

[103] F. Abyarjoo, A. Barreto, J. Cofino, and F. R. Ortega, “Implementing a sensor fusion algorithm for 3d orientation detection with inertial/magnetic sensors,” in *Innovations and advances in computing, informatics, systems sciences, networking and engineering.* Springer, 2015, pp. 305–310.

[104] W. Y. Wong and M. S. Wong, “Trunk posture monitoring with inertial sensors,” *European Spine Journal*, vol. 17, no. 5, pp. 743–753, 2008.

[105] N. Rösch, *Rotations, Quaternions and Double Groups. By Simon L. Altmann, Clarendon Press, Oxford, 1986, 317 Pp.*, 1987, vol. 32.

[106] G. Q. Xing and S. A. Parvez, “Alternate forms of relative attitude kinematics and dynamics equations,” 2001.

[107] P. S. Maybeck, *Stochastic models, estimation, and control.* Academic press, 1979, vol. 1.

[108] F. L. Markley and J. L. Crassidis, *Fundamentals of Spacecraft Attitude Determination and Control*, ser. Space Technology Library. New York, NY: Springer New York, 2014, vol. 33.

[109] H. M. T. Menegaz and J. Y. Ishihara, “Unscented and square-root unscented Kalman filters for quaternionic systems,” *International Journal of Robust and Nonlinear Control*, vol. 28, no. 15, pp. 4500–4527, 2018.

[110] S. J. Julier, J. K. Uhlmann, and H. F. Durrant-Whyte, “A new approach for filtering nonlinear systems,” in *Proceedings of 1995 American Control Conference - ACC’95*, vol. 3, Jun. 1995, pp. 1628–1632 vol.3.

[111] F. Pedregosa, G. Varoquaux, A. Gramfort, V. Michel, B. Thirion, O. Grisel, M. Blondel, P. Prettenhofer, R. Weiss, V. Dubourg, J. Vanderplas, A. Passos, D. Cournapeau, M. Brucher, M. Perrot, and E. Duchesnay, “Scikit-learn: Machine learning in Python,” *Journal of Machine Learning Research*, vol. 12, pp. 2825–2830, 2011.

[112] M. Paulich, M. Schepers, N. Rudigkeit, and G. Bellusci, “Xsens mtw awinda: Miniature wireless inertial-magnetic motion tracker for highly accurate 3d kinematic applications,” *Unpublished*, 2018. [Online]. Available: http://rgdoi.net/10.13140/RG.2.2.23576.49929

[113] J. L. McGinley, R. Baker, R. Wolfe, and M. E. Morris, “The reliability of three-dimensional kinematic gait measurements: a systematic review,” *Gait & posture*, vol. 29, no. 3, pp. 360–369, 2009.

[114] E. Charry, M. Umer, and S. Taylor, “Design and validation of an ambulatory inertial system for 3-d measurements of low back movements,” in *2011 Seventh International Conference on Intelligent Sensors, Sensor Networks and Information Processing.* IEEE, 2011, pp. 58–63.